

1 **Tropospheric vertical column densities of NO<sub>2</sub> over managed dryland ecosystems**  
2 **(Xinjiang, P. R. China): MAX-DOAS measurements vs. 3-D dispersion model**  
3 **simulations based on laboratory derived NO emission from soil samples**

4

5 Buhalgem Mamtimin<sup>1\*</sup>, Thomas Behrendt<sup>1</sup>, Moawad M. Badawy<sup>1,2</sup>, Thomas Wagner<sup>1</sup>, Yue  
6 Qi<sup>1,3</sup>, Zhaopeng Wu<sup>1,4</sup> and Franz X. Meixner<sup>1</sup>

7

8 <sup>1</sup>*Max Planck Institute for Chemistry, Mainz, Germany.*

9 <sup>2</sup>*Department of Geography, Faculty of Arts, Ain-Shams University, Egypt.*

10 <sup>3</sup>*International Cooperation Department, National Center for Climate Change Strategy and*  
11 *International Cooperation, Beijing, P. R. China.*

12 <sup>4</sup>*Institute of Geography Science, Xinjiang Normal University, China.*

13

14 \*Corresponding author: buhalgem.mamtimin@mpic.de

15

16

17

18

19

20 **Abstract**

21 We report on MAX-DOAS observations of NO<sub>2</sub> over an oasis-ecotone-desert ecosystem in  
22 NW-China. There, local ambient NO<sub>2</sub> concentrations originate from enhanced biogenic NO  
23 emission of intensively managed soils. Our target oasis “Milan” is located at the southern  
24 edge of the Taklimakan desert, very remote and well isolated from other potential anthropoge-  
25 nic and biogenic NO<sub>x</sub> sources. Four observation sites for MAX-DOAS measurements were  
26 selected, at the oasis center, downwind and upwind of the oasis, and in the desert. Biogenic  
27 NO emissions in terms of (i) soil moisture and (ii) soil temperature of Milan oasis’ (iii)  
28 different land-cover type sub-units (cotton, Jujube trees, cotton/Jujube mixture, desert) were  
29 quantified by laboratory incubation of corresponding soil samples. Net potential NO fluxes  
30 were up-scaled to oasis scale by areal distribution and classification of land-cover types  
31 derived from satellite images using GIS techniques. A Lagrangian dispersion model (LASAT,  
32 Lagrangian Simulation of Aerosol-Transport) was used to calculate the dispersion of soil  
33 emitted NO into the atmospheric boundary layer over Milan oasis. Three dimensional NO  
34 concentrations (30 m horizontal resolution) have been converted to 3-D (three dimensional)  
35 NO<sub>2</sub> concentrations, assuming photostationary state conditions. NO<sub>2</sub> column densities were  
36 simulated by suitable vertical integration of modeled 3-D NO<sub>2</sub> concentrations at those  
37 downwind and upwind locations, where the MAX-DOAS measurements were performed.  
38 Downwind-upwind differences (a direct measure of Milan oasis’ contribution to the areal  
39 increase of ambient NO<sub>2</sub> concentration) of measured and simulated slant (as well as vertical)  
40 NO<sub>2</sub> column densities show excellent agreement. This agreement is considered as the first  
41 successful attempt to prove the validity of the chosen approach to up-scale laboratory derived  
42 biogenic NO fluxes to ecosystem field conditions, i.e. from the spatial scale of a soil sample  
43 (cm<sup>2</sup>) to the size of an entire agricultural ecosystem (km<sup>2</sup>).

44

45

## 46 **1 Introduction**

47 Emissions of nitric oxide (NO) are important in regulating chemical processes of the atmo-  
48 sphere (Crutzen, 1987). Once emitted into the atmosphere, NO reacts rapidly with ozone (O<sub>3</sub>)  
49 to nitrogen dioxide (NO<sub>2</sub>) which, under daylight conditions, is photolyzed back to NO ( $\lambda \leq$   
50 420 nm). For that reason, NO and NO<sub>2</sub> are usually considered as NO<sub>x</sub> (NO<sub>x</sub> = NO + NO<sub>2</sub>).  
51 Ambient NO<sub>x</sub> is a key catalyst in atmospheric chemistry: during the atmospheric oxidation of  
52 hydrocarbons its ambient concentration determines whether ozone (O<sub>3</sub>) is photochemically  
53 generated or destroyed in the troposphere (Chameides et al., 1992). While the combustion of  
54 fossil fuels (power plants, vehicles) is still the most important global NO<sub>x</sub> source (approx. 25  
55 Tg a<sup>-1</sup> in terms of mass of N), biogenic NO emissions from soils have been estimated to range  
56 between 6.6 and 9.6 Tg a<sup>-1</sup> (Denman et al., 2007). The considerable uncertainty about the  
57 range of soil biogenic NO emissions stems from widely differing estimates of the NO  
58 emission. Moreover, the uncertainties in the NO emission data from semi-arid, arid, and  
59 hyper-arid regions are very large (mainly due to a very small number of measurements being  
60 available). These ecosystems, however, are considered to contribute more than half to the  
61 global soil NO source (Davidson and Kinglerlee, 1997), and make approx. 40% of planet  
62 Earth's total land surface (Harrison and Pearce, 2000).

63 Production (and consumption) of NO in the soil depends mainly on soil microbial activity and  
64 is mainly controlled by soil temperature, soil moisture, and soil nutrient concentration  
65 (Conrad, 1996; Meixner and Yang 2006; Ludwig et al., 2001). Any natural or anthropogenic  
66 action that result in the inputs of nutrients (e.g. by fertilizer application) and/or modification  
67 of soil nutrient turnover rates has a substantial effect on soil biogenic NO emission. The rapid  
68 (economically driven) intensification of arid agriculture (oasis agriculture), particularly by en-  
69 largement of the arable area and by enhancement of necessary irrigation leads inevitably to  
70 the increase of soil biogenic NO emissions. Since those microbial processes which underlay  
71 NO production and NO consumption in soils are confined to the uppermost soil layers  
72 (<0.05 m depth, Rudolph et al., 1996), the most direct method for their characterization and  
73 quantification is usually realized by laboratory incubation of soil samples; corresponding  
74 measurements result in the determination of so-called net potential NO fluxes, which are  
75 explicit functions of soil moisture, soil temperature, and ambient NO concentration (Behrendt  
76 et al., 2014).

77 Tropospheric NO<sub>2</sub> column densities can be retrieved from satellite observations using  
78 differential optical absorption spectroscopy (DOAS) (e.g. Leue et al., 2001; Richter and

79 Burrows, 2002, Beirle et al., 2004). Identification and quantification of the sources of  
80 tropospheric NO<sub>2</sub> column densities are important for monitoring air quality, for understanding  
81 radiative forcing and its impact on local climate. Ground-based Multi Axis Differential  
82 Optical Absorption Spectroscopy (MAX-DOAS) is a novel measurement technique  
83 (Hönninger et al., 2004) that represents a significant advantage over the well-established  
84 zenith scattered sunlight DOAS instruments, which are mainly sensitive to stratospheric  
85 absorbers. From NO<sub>2</sub> slant column densities, retrieved from measurements at different  
86 elevation angles, information about tropospheric NO<sub>2</sub> profiles and/or tropospheric vertical  
87 column densities can be obtained (e.g. Sinreich et al., 2005; Wittrock et al., 2004; Wagner et  
88 al., 2011).

89 In this paper we concentrate (a) on ground-based MAX-DOAS measurements of slant and  
90 vertical NO<sub>2</sub> column densities over an intensively used oasis of the Taklimakan desert (NW-  
91 China), (b) on biogenic NO emissions derived from laboratory incubation measurements on  
92 oasis soil samples, (c) on up-scaling of the laboratory results to the oasis level, (d) calculation  
93 of atmospheric boundary layer NO<sub>2</sub> concentrations by suitable NO→NO<sub>2</sub> conversion and  
94 3 dimensional dispersion modelling, and (e) on simulating slant and vertical NO<sub>2</sub> column den-  
95 sities from the calculated 3-D-NO<sub>2</sub> distributions by integration along the MAX-DOAS light  
96 path. The final aim is comparison and discussion of the results obtained under (a) and (e).

97

## 98 **2 Materials and methods**

### 99 **2.1 Research area**

100 After two ‘searching field campaigns’ (2008 and 2009) in the Xinjiang Uighur Autonomous  
101 Region of NW-China, the oasis “Milan” has been identified as the target oasis for the  
102 presented research. The contemporary oasis Milan, identical to the ancient silk-road post  
103 “Miran”, belongs to the county “Ruoqiang” of the Xinjiang province and is located in the  
104 southern Taklimakan Desert on the foot of the Altun Shan Mountains (39.25 °N, 88.92 °E,  
105 998 m a.s.l.). In the early 1950s, the delta-shaped oasis (see Fig. 1) has been established as an  
106 agricultural co-operative “state farm” (*Xinjiang Production and Construction Crop*) and  
107 covers nowadays about 100 km<sup>2</sup>. Milan oasis can be geomorphologically classified as a  
108 “mountain-oasis-ecotone-desert system (MOED system)” consisting of Gobi (gravel) desert, a  
109 salty transition zone surrounding the oasis, and dryland farming with irrigation. The latter  
110 consists only of two crops, cotton and jujube trees (*Ziziphus Jujuba* L., “red date”), which are  
111 planted, irrigated, and fertilized following standardized protocols and growing on rectangular

112 fields (approx. 10 ha) of pure cultures or mixtures of it. The general energy supply of Milan  
113 oasis is entirely provided by nearby hydropower plants, and battery powered trikes dominate  
114 the local public and private transport. Consequently, anthropogenic  $\text{NO}_x$  emissions of Milan  
115 oasis are considered as very low, if not negligible. Beyond that, Milan oasis is isolated by the  
116 desert from neighbouring oases by 80 to 400 km. Therefore, the dominant  $\text{NO}_x$  source of Mi-  
117 lan oasis are biogenic NO emissions from its intensively managed crop fields; the oasis can be  
118 undoubtedly considered as a large "hotspot in the middle of nothing". Given this very specific  
119 situation, it is certainly justified to assume that (a)  $\text{NO}_2$  concentrations in the atmospheric  
120 boundary layer over Milan oasis are only caused by the oasis itself, and (b) free tropospheric  
121  $\text{NO}_2$  concentrations, which are usually due to large-scale tropospheric  $\text{NO}_2$  advection, are  
122 negligible.

123 According to Koeppen classification (Koeppen, 1931; Kottek et al., 2006), Milan oasis owns  
124 a cold desert climate (BWk), which is dominated by long hot summers (30 years' mean:  
125  $29^\circ\text{C}$ ) and cold winters (30 years' mean:  $-6^\circ\text{C}$ ). Mean annual precipitation amounts  
126 28.5 mm, mean annual evaporating capacity is 2920 mm, mean wind direction is NE to E, and  
127 mean wind speed is  $2.7 \text{ m s}^{-1}$ .

## 128 **2.2 *In-situ* measurements**

129 A field campaign has been performed at Milan oasis, from 24 May to 26 June, 2011. A total  
130 of 32 individual MAX-DOAS measurements (approx. 20 min) have been performed by two  
131 Mini-MAX-DOAS instruments (partially simultaneously) on 21 days during the 2011 cam-  
132 paign at the NE natural forest site (1), desert site (2), jujube site (3) and hotel station in Milan  
133 oasis center (4). Accompanying data of wind direction, wind speed, air temperature,  
134 barometric pressure, global and net radiation have been observed at sites (1) – (5) at 1.8 m  
135 above ground (at NE natural forest: 11 m; at hotel station: 23 m). Soil temperature (at 0.05 m  
136 depth), as well as rainfall (amount and intensity) were recorded at all sites in 2011.

### 137 **2.2.1 Ground-based measurements of vertical column densities of $\text{NO}_2$**

138 Multi-Axis-Differential Optical Absorption Spectroscopy (MAX-DOAS) observes scattered  
139 sun light under various (mostly slant) elevation angles. From combinations of the retrieved  
140  $\text{NO}_2$  slant column densities (SCDs) obtained at different elevation angles, information on the  
141 vertical  $\text{NO}_2$  profile and/or on the corresponding vertical column density (VCD) can be  
142 obtained (e.g. Hönninger et al., 2002; Sinreich et al., 2005; Wittrock et al., 2004; Wagner et  
143 al., 2011). Spectral calibration of the MAX-DOAS instruments was performed by fitting a

144 measured spectrum to a convoluted solar spectrum based on a high resolution solar spectrum  
 145 (Kurucz et al., 1984). Several trace gas absorption cross sections of NO<sub>2</sub> at 294 K (Vandaele  
 146 et al., 1996), H<sub>2</sub>O at 290 K (Rothman et al., 2005), Glyoxal at 296 K (Volkamer et al., 2005),  
 147 O<sub>3</sub> at 243 K (Bogumil et al., 2003) and O<sub>4</sub> at 286K (Hermans et al., 1999) were convolved to  
 148 match the resolution of the instrument and then used in the spectral analysis using a  
 149 wavelength range of 420-450 nm (also a Ring spectrum was included in the fitting process).  
 150 The output of the spectral analysis is the NO<sub>2</sub> SCD, which represents the NO<sub>2</sub> concentration  
 151 integrated along the corresponding light paths through the atmosphere.  
 152 Since a spectrum measured in zenith direction (a so called Fraunhofer reference spectrum) is  
 153 included in the fit process to remove the strong Fraunhofer lines, the retrieved NO<sub>2</sub> SCD ac-  
 154 tually represents the difference between the SCDs of the measurement and the Fraunhofer  
 155 reference spectrum; it is usually referred to as differential SCD or DSCD<sub>meas</sub>. The tropospheric  
 156 DSCD for the elevation angle  $\alpha$  can be derived from MAX-DOAS observation by subtract-  
 157 ing the NO<sub>2</sub> DSCD for the closest zenith observation ( $\alpha_0 = 90^\circ$ ):

$$158 \quad DSCD_{trop}(\alpha) = DSCD_{meas}(\alpha) - DSCD_{meas}(\alpha_0) \quad (1)$$

159 DSCDs are converted into VCDs (the vertically integrated concentration) using so called air  
 160 mass factors (AMF, Solomon et al., 1987), which is defined by:

$$161 \quad AMF = SCD / VCD \quad (2)$$

162

163 In many cases AMF are determined from radiative transfer simulations (Solomon et al.,  
 164 1987). However, if trace gas column densities are retrieved from MAX-DOAS observations at  
 165 high elevation angles ( $> 10^\circ$ ), the AMF can be determined by the so called geometric approxi-  
 166 mation (Hönninger et al., 2002; Brinkma et al., 2008; Wagner et al., 2010):

$$167 \quad AMF_{trop} \approx \frac{1}{\sin(\alpha)} \quad (3)$$

168

169 In this study, the tropospheric vertical column density (VCD<sub>trop</sub>) is obtained from DSCD<sub>trop</sub>( $\alpha$ )  
 170 as discussed by Wagner et al. (2010):

$$171 \quad VCD_{trop} = \frac{DSCD_{trop}(\alpha)}{AMF_{trop}(\alpha - AMF_{trop}(\alpha_0))} \quad (4)$$

172 During the field experiments, the MAX-DOAS instruments have been mounted on solid  
173 tables (aluminium structure) at approx. 11 m a.gr. (NW natural forest, hotel station) and 3.5 m  
174 a.gr. (remainder of sites) with the telescope facing northwards. Observations were always  
175 made on elevation angles of 0°, 2°, 4°, 6°, 8°, 10°, 15°, 20°, 45° and 90°.  $VCD_{tropS}$  were  
176 determined from measurements at 15°. The potential importance of scattering on the  
177 interpretation of the MAX-DOAS measurements depends on two main aspects: first on the  
178 height of the trace gas layer and second on the amount of aerosols. In our case the trace gas  
179 layer is shallow and the aerosol amount is low (see 2.2.8). Thus scattering effects can be  
180 neglected. However, for comparison of the  $DSCD_{trop}$  data obtained by MAX-DOAS with the  
181 simulated SCDs obtained from 3 D distributions of  $NO_2$  concentration (calculated with  
182 LASAT (Lagrangian Simulation of Aerosol-Transport)) on the basis of laboratory derived net  
183 potential  $NO_2$  fluxes) the lower elevation angles (2°, 4°) for  $DSCD_{trop}(\alpha)$  have been used,  
184 which have a much higher sensitivity to the observed  $NO_2$ .  
185 For classifying all MAX-DOAS measurements whether they were made up-wind, down-wind,  
186 or in the center of Milan oasis, their observation position was related to the mean wind  
187 direction during each measurement period. Wind measurements were part of accompanying  
188 *in-situ* measurements (see below).

## 189 **2.2.2 Accompanying measurements**

190 Wind direction, wind speed, air temperature, relative humidity, barometric pressure, and  
191 rainfall intensity have been measured by combined weather sensors (weather transmitter  
192 WXT510, Vaisala, Finland). All five weather sensors have been operated side-by-side for one  
193 week before they have been mounted at the individual measurement sites (1) – (5). Based on  
194 these results, all meteorological data, which have been measured between 3 – 24 July, 2011  
195 have been corrected using one of the sensors as reference. All combined weather sensors'  
196 data, as well as those of net radiation (4 component net radiation sensor, model NR01,  
197 Hukseflux, The Netherlands) and soil temperature (thermistor probe, model 109, Campbell  
198 Scientific, U.S.A.) have been recorded every minute. Ambient  $O_3$  concentrations and  $NO_2$   
199 photolysis rates have also been measured in-situ; both quantities are necessary to calculate the  
200  $NO \rightarrow NO_2$  conversion factor (see Sect. 2.2.8). Ozone concentrations have been measured by  
201 UV-absorption spectroscopy (model 49i, ThermoFisher Scientific, U.S.A.) and  $NO_2$  photoly-  
202 sis rate by a filter radiometer (model 2-Pi-J $NO_2$ , metcon, Germany) in 1 minute intervals.

## 203 **2.2.3 Soil samples**

204 Microbial processes responsible for biogenic NO emission are confined to the uppermost soil  
205 layers (Galbally and Johansson, 1989; Rudolph et al., 1996; Rudolph and Conrad, 1996).  
206 Consequently, composite soil samples (1 kg of top soil, 0–5 cm depth) have been collected at  
207 the individual sites of Milan oasis (natural forest, cotton, jujube, cotton & jujube mixture,  
208 desert). All samples (air dried) were sent from Xinjiang to Germany by air cargo and stored  
209 refrigerated (+ 4°C) until laboratory analysis of the net potential NO flux (see below). Sub-  
210 samples have been analyzed for dry bulk soil density (ISO 11272), pH (ISO 10390), electrical  
211 conductivity (salinity, ISO 11265), contents of nitrate and ammonium (ISO 14256), total  
212 carbon and total nitrogen (ISO 10649 and ISO 13878), texture (ISO 11277), as well of soil  
213 water potential (pF values 1.8, 2.5, 4.2, Hartge and Horn, 2009).

214 Electrical conductivity varied between 1.6 to 9.5 dS m<sup>-1</sup> within the managed soils, and was  
215 59.8 and 3.0 dS m<sup>-1</sup> in the natural forest and desert soils, respectively. Commercially available  
216 soil moisture probes (e.g. TDR (Time-Domain-Reflectometry) and FDR (Frequency-Domain-  
217 Reflectometry)) show extreme interferences for soils of >2 dS m<sup>-1</sup> (c.f. Kargas et al., 2013)  
218 and their calibration for such soils is extremely challenging, if possible at all. Indeed, FDR-  
219 signals monitored in Milan oasis' soils were extremely noisy and spurious. Nevertheless, up-  
220 scaling of the laboratory derived net potential NO fluxes needs data of the uppermost layer of  
221 each soil of Milan oasis land-types (see Sect. 2.2.6). For that, as most reasonable  
222 approximation, it was decided to use that individual (constant) gravimetric soil moisture  
223 content, which corresponds to the so-called “wilting point”. The latter was determined by  
224 laboratory water tension measurements (pF 4.2) on undisturbed soil cores from each land-  
225 cover type. The wilting point is defined as that soil moisture in the root zone, which would  
226 cause irreversible wilting of plants. Wilting point conditions in the uppermost soil layers  
227 (2 cm) of soils in the Taklimakan Desert are easily reached, since evaporation is extremely  
228 high (evaporating capacity 2920 mm a<sup>-1</sup>). Even after flooding irrigation of Milan oasis' crop  
229 fields, these conditions have repeatedly been observed within at least 3 days by visual  
230 inspections.

#### 231 **2.2.4 Laboratory determination of net potential NO fluxes**

232 The methodology for the laboratory measurement of the NO flux from soil has been deve-  
233 loped at the end of the nineties (Yang and Meixner, 1997) and has been continuously used  
234 during the last two decades (Otter et al., 1999; Kirkman et al., 2001; van Dijk and Meixner,  
235 2001; Feig et al., 2008a; Feig et al., 2008b; Yu et al., 2008; Ashuri, 2009; Feig, 2009; Gelfand  
236 et al., 2009; Yu et al., 2010a, 2010b; Bargsten et al., 2010). The methodology has been

237 significantly improved in the frame of this study and is described in detail by Behrendt et al.  
238 (2014).

239 Generally, the release of gaseous NO from soil is the result of microbial NO production and  
240 simultaneous NO consumption. The latter is, as shown by Behrendt et al. (2014), particularly  
241 for arid and hyper-arid soils, negligible. Applying the laboratory dynamic chamber method,  
242 the release of NO is determined by incubating aliquots of the soil samples in a dynamic  
243 chamber system under varying, but prescribed conditions of soil moisture, soil temperature,  
244 and chamber's headspace NO concentrations. From the difference of measured NO concentra-  
245 tions at the outlets of each soil containing chamber and an empty reference chamber, actual  
246 net potential NO fluxes (in terms of mass of nitric oxide per area and time) is calculated as  
247 function of soil moisture and soil temperature. For that, a known mass (approx. 60 g dry  
248 weight) of sieved (2 mm) and wetted (to water holding capacity) soil is placed in one of six  
249 Plexiglas chambers (volume  $9.7 \times 10^{-4} \text{ m}^3$ ) in a thermo-controlled cabinet (0 – 40°C). After  
250 passing through a purification system (PAG 003, Ecophysics, Switzerland), dry pressurized,  
251 zero (i.e., "NO free") air is supplied to each chamber, controlled by a mass flow controller  
252 ( $4.167 \times 10^{-5} \text{ m}^3 \text{ s}^{-1}$ ). The outlet of each chamber is connected via a switching valve system to  
253 the gas-phase chemiluminescence NO analyzer (model 42i-TL, Thermo Fisher Scientific Inc.,  
254 U.S.A.) and to the non dispersive infrared analyzer CO<sub>2</sub>/H<sub>2</sub>O-analyzer (model LI-COR 840A,  
255 LI-COR Biosciences Inc., U.S.A.). During a period of 24 – 48 h, the soil samples are slowly  
256 drying out, hence providing the desired variation over the entire range of soil moisture (i.e.  
257 from water holding capacity to wilting point conditions and completely dry soil). During the  
258 drying out period, the temperature of thermo-controlled cabinet is repeatedly changed from 20  
259 to 30°C, hence providing the desired soil temperature variation (Behrendt et al. 2014). Occa-  
260 sionally, nitric oxide standard gas (200 ppm) is diluted into the air purification system via a  
261 mass flow controller; this allows the control of the chamber headspace NO concentration  
262 when determining NO consumption rate of the soil sample. The actual soil moisture content  
263 of each soil sample is determined by considering the H<sub>2</sub>O mass balance of each chamber,  
264 where the temporal change of the chamber's headspace H<sub>2</sub>O concentration is explicitly related  
265 to the evaporation rate of the soil sample. Tracking the chamber's headspace H<sub>2</sub>O concen-  
266 tration throughout the drying-out period and relating it to the gravimetrically determined total  
267 soil mass at the start and end of the measurement period delivers the actual gravimetric soil  
268 moisture content of the soil sample (Behrendt et al., 2014).

269 As shown during the last two decades (Yang and Meixner, 1997; Otter et al., 1999; Kirkman  
270 et al., 2001; van Dijk and Meixner, 2001; van Dijk et al., 2002; Meixner and Yang, 2006; Yu

271 et al., 2008, 2010; Feig et al., 2008; Ashuri, 2009; Feig, 2009; Gelfand et al., 2009 and  
 272 Bargsten et al., 2010), the dependence of NO release from gravimetric soil moisture and soil  
 273 temperature can be characterized by two explicit dimensionless functions, the so-called opti-  
 274 mum soil moisture curve  $g(\theta_g)$  and the exponential soil temperature curve  $h(T_{soil})$

$$275 \quad g(\theta_g) = \left( \frac{\theta_g}{\theta_{g,0}} \right)^a \exp \left[ -a \left( \frac{\theta_g}{\theta_{g,0}} - 1 \right) \right] \quad (5)$$

$$276 \quad h(T_{soil}) = \exp \left[ \frac{\ln Q_{10,NO}}{10} (T_{soil} - T_{soil,0}) \right] \quad (6)$$

277 where  $\theta_g$  is the dimensionless gravimetric soil moisture content,  $\theta_{g,0}$  the so-called optimum  
 278 gravimetric soil moisture content (i.e., where the maximum NO release has been observed),  $a$   
 279 is the soil moisture curve's shape factor (solely derived from NO release and gravimetric soil  
 280 moisture data which have been observed during the drying-out measurements, see Behrendt et  
 281 al. 2014),  $T_{soil}$  is the soil temperature (in °C),  $T_{soil,0}$  is the reference temperature (here: 20°C),  
 282 and  $Q_{10,NO}$  is the (logarithmic) slope of  $h(T_{soil})$ , defined by

$$283 \quad Q_{10,NO} = \frac{\ln F_{NO}(\theta_{g,0}, T_{soil,1}) - \ln F_{NO}(\theta_{g,0}, T_{soil,0})}{T_{soil,1} - T_{soil,0}} \quad (7)$$

284 where  $T_{soil,1}$  is a soil temperature which is 10 K different from  $T_{soil,0}$  (here: 30°C). The actual  
 285 NO fluxes  $F_{NO}$  ( $\text{ng m}^{-2} \text{s}^{-1}$ ; in terms of mass of nitric oxide) are defined by

$$286 \quad F_{NO}(\theta_{g,0}, T_{soil,0}) = \frac{Q}{A_{soil}} [m_{NO, \text{cham}}(\theta_{g,0}, T_{soil,0}) - m_{NO, \text{ref}}] f_{C,NO} \quad (8)$$

$$287 \quad F_{NO}(\theta_{g,0}, T_{soil,1}) = \frac{Q}{A_{soil}} [m_{NO, \text{cham}}(\theta_{g,0}, T_{soil,1}) - m_{NO, \text{ref}}] f_{C,NO} \quad (9)$$

288 where  $Q$  is the purging rate of the dynamic chambers ( $\text{m}^3 \text{s}^{-1}$ ),  $A_{soil}$  is the cross-section of the  
 289 dynamic chamber ( $\text{m}^2$ ), and  $m_{NO, \text{cham}}$  and  $m_{NO, \text{ref}}$  are the NO mixing ratios (ppb) observed un-  
 290 der conditions  $(\theta_{g,0}, T_{soil,0})$  and  $(\theta_{g,0}, T_{soil,1})$  at the outlets of each soil chamber and the reference  
 291 chamber, respectively. The conversion of NO mixing ratios to corresponding NO concentra-  
 292 tions ( $\text{ng m}^{-3}$ , in terms of mass of nitric oxide) is considered by  $f_{C,NO}$  ( $= 572.5 \text{ ng m}^{-3} \text{ ppb}^{-1}$   
 293 under STP conditions). Finally, the net potential NO flux,  $F_{NO}(\theta_g, T_{soil})$  is given by

$$294 \quad F_{NO}(\theta_g, T_{soil}) = F_{NO}(\theta_{g,0}, T_{soil,0}) g(\theta_g) h(T_{soil}) \quad (10)$$

295 This net potential NO flux is specific for each soil sample, hence for sites (1), (2), (4), and (5)  
296 of Milan oasis; the actual NO flux of the sites is calculated applying corresponding field data  
297 of gravimetric soil moisture and soil temperature. This procedure has been successfully  
298 applied for a variety of terrestrial ecosystems (e.g., Otter et al., 1999; van Dijk et al., 2002;  
299 Ganzeveld et al., 2008). For soils of the Zimbabwean Kalahari (Ludwig et al., 2001; Meixner  
300 and Yang, 2006), for a German grassland soil (Mayer et al., 2011), but also for Brazilian  
301 rainforest soils (van Dijk et al, 2002), soil biogenic NO fluxes derived from the described  
302 laboratory incubation method have been successfully verified by field measurements using  
303 both, field dynamic chamber and micrometeorological (aerodynamic gradient) techniques.

### 304 **2.2.5 Classification and actual distribution of Milan fields**

305 Image classification is likely to assemble groups of identical pixels found in remotely sensed  
306 data into classes that match the informational categories of user interest by comparing pixels  
307 to one another and to those of known identity. For the purposes of our study, land-cover  
308 classification was carried out based on two Quickbird images (0.6 m ground resolution,  
309 DigitalGlobe, <http://www.digitalglobe.com>) acquired on 09 April and 31 August 2007  
310 respectively, with the aid of a recent ETM+ Landsat image (141/033,  
311 <http://earthexplorer.usgs.gov/>) acquired on 25 April 2011 (15 and 30 m spatial resolution). A  
312 major advantage of using Quickbird images of high spatial resolution images is that such data  
313 greatly reduce the mixed-pixel problem (a “mixed pixel” consists of several land-cover  
314 classes) and provide a greater potential to extract much more detailed information on land-  
315 cover structures (e.g. field borders, buildings, roads) than medium or coarse spatial resolution  
316 data using whether on screen digitizing or image classification.

317 However, we take the advantage of resolution merge processing to increase the spatial  
318 resolution of the Landsat image from 30 to 15 meters for the bands 1-5 and 7 for better land-  
319 cover mapping and for updating the land-cover map from 2007 to 2011. Then, we defined  
320 different areas of interests (AOIs) to represent the major land-covers with the aid of in-situ  
321 GPS data collection (45 points). Next, we increased number of AOIs based on image spectral  
322 analysis method. After that supervised classification was performed using the maximum  
323 likelihood parametric rule and probabilities. This classifier uses the training data by means of  
324 estimating means and variances of the classes, which are used to estimate Bayesian  
325 probability and also consider the variability of brightness values in each class. For that, it is  
326 the most powerful classification method when accurate training data is provided and one of  
327 the most widely used algorithms (Perumal and Bhaskaran, 2010). As a result, five major

328 ecosystems were determined: cotton, jujube, cotton/ujube mixture fields, desert, and plant  
329 cover. The cotton and the jujube fields are the most dominant types. Finally, the classified  
330 land-cover image was converted into vector format using polygon vector data type to be  
331 implemented in LASAT analysis as sources of NO flux and for the purpose of estimating NO  
332 concentrations. The map includes 2500 polygons of different sizes as sub-units of Milan  
333 major land-cover.

#### 334 **2.2.6 Two dimensional distribution of soil NO emissions of Milan oasis**

335 The soil NO emission sources of Milan oasis were defined by individual source units, which  
336 have been identified as those sub-units (polygons) of the land-cover vector map consisting of  
337 natural forest or desert, or covered by cotton, jujube, cotton/ujube mixture. Two identifiers  
338 have been attributed to each source unit, (a) a metric coordinate whose numerical format re-  
339 fers to the corner of the corresponding polygon, and (b) a unique ID number followed by a de-  
340 scription of its land cover type. The soil NO source strength (i.e., actual NO flux, see Sect.  
341 2.2.4) of each source unit has been calculated from the corresponding net potential NO flux,  
342 the land-cover type specific gravimetric soil moisture content (“wilting point”), and the actual  
343 soil temperature, which has been *in-situ* measured for each of the land-cover types of Milan  
344 oasis (see Sect. 2.2.2). Those polygons which are not matching the mentioned land-cover  
345 types and other tiny polygons generated by digital image processing techniques were  
346 dismissed to avoid intricate geometric errors affecting NO emission data. In other words,  
347 these “other classes” were dissolved before performing LASAT analysis to avoid extreme  
348 values.

#### 349 **2.2.7 Three dimensional distribution of NO concentrations by Lagrangian dispersion** 350 **modelling (LASAT)**

351 Having the actual NO source units of the Milan oasis available, the 3-D distribution of NO  
352 concentrations in the atmospheric boundary layer (0 – 1500 m a.gr.) over Milan oasis have  
353 been calculated by the Lagrangian dispersion model LASAT (German VDI Guidelines  
354 VDI3945, part 3; c.f. Janicke Consulting, 2011). LASAT is a state-of-the-art model, since (a)  
355 LASAT is one of those transport-dispersion models of air-pollution which is officially  
356 licensed for legal use of environmental issues (in Germany), and (b) among comparable  
357 micro-scale (e.g. street canyons) transport-dispersion models LASAT considers at least  
358 chemical transformations of 1<sup>st</sup> order and keeps nonetheless truly operational. Being a  
359 transport-dispersion-model, LASAT basically considers advection (“pixel cross-talk”)

360 applying the 3D-continuity equation for any chosen tracer (see German VDI Guidelines  
361 VDI3945, part 3, cf. Janicke Consulting, 2011). For that, pre-processing of meteorological pa-  
362 rameters (i.e. 3-D wind distributions, based on meteorological in-situ measurements, see Sect.  
363 2.2.2) and calculation of dispersion parameters ( $\sigma_y$ ,  $\sigma_z$ ) have to be performed. Unfortunately,  
364 it was difficult to obtain fine resolution using LASAT individually. Therefore, LASAT model  
365 was integrated with Geographic Information System (ArcGIS) by using an advanced module  
366 namely LASarc (IVU Umwelt GmbH, 2012). LASarc allowed us to calculate NO  
367 concentrations using relatively fine resolution of 30m×30m and taking the advantages of  
368 using integrated map colour scheme in ArcGIS. This module has been used to realize Milan  
369 oasis' complex NO source configuration and to setup calculations of LASAT.

370 The model was designed to calculate NO-concentrations at 16 different vertical layers (0–3,  
371 3–5, 5–10, 10–20, 20–30, 30–50, 50–70, 70–100, 100–150, 150–200, 200–300, 300–400,  
372 400–500, 500–700, 700–1000, and 1000–1500 m a.gr.). The horizontal resolution is 30 m, in  
373 x-direction (W-E) as well in y-direction (S-N), which results in 656 (x) and 381 (y) grids for  
374 the Milan oasis domain. LASAT's meteorological input data contain a variety of parameters,  
375 namely start and end time ( $T_1$ ,  $T_2$ ), wind speed ( $U_a$ ) and wind direction ( $R_a$ ) at anemometer  
376 height ( $H_a$ ), average surface roughness ( $Z_0$ ), and atmospheric stability (in terms of stability  
377 classes). These parameters have been provided in a time-dependent tabular form, up-dated  
378 every 30 minutes (except  $Z_0$ ). Average (30 min) wind speed and wind direction data have  
379 been calculated from *in-situ* measurements (1 min resolution, see Sect. 2.2.2).

380 LASAT's pre-processing module determines the vertical profile of wind speed according to  
381 the well-known logarithmic relation,

$$382 \quad U(z) = \frac{u_*}{k} \ln\left(\frac{z}{Z_0}\right) \quad (11)$$

383 where  $U(z)$  is the horizontal wind speed ( $\text{m s}^{-1}$ ) at height  $z$  (m),  $u_*$  is the friction velocity  
384 ( $\text{m s}^{-1}$ ),  $k$  is the dimensionless von Karman constant ( $= 0.4$ , Simiu and Scanlan, 1996), and  $Z_0$   
385 is the surface roughness length (m). LASAT's pre-processing module accepts only one indivi-  
386 dual value for  $Z_0$ ; nevertheless, the required mean value has been calculated from all  $Z_0$ 's of  
387 Milan oasis domain, which have been assigned to each of the sub-units (polygons) of the  
388 vector land-cover map (see Sect. 2.2.5). For individual  $Z_0$ 's, we calculated land-cover specific  
389 NDVI data (normalized differential vegetation index) from Landsat ETM+ image (141/033)

390 
$$NDVI = \frac{r_{NIR} - r_{RED}}{r_{NIR} + r_{RED}} \quad (12)$$

391 where *NIR* is the reflectance in the near-infrared bandwidth (0.77-0.90 μm) and *RED* is the  
 392 reflectance in the red bandwidth (0.63-0.69 μm). In Landsat ETM+ images, these correspond  
 393 to bands 4 and 3, respectively. Finally,  $r_{NIR}$  and  $r_{RED}$  are the corresponding ratios of reflected  
 394 and incident energy as a function of wavelength (see Chander and Markham, 2003). Then,  
 395 surface roughness grid data was estimated as:

396 
$$Z_0(x, y) = \exp(a_{xy} NDVI(x, y) + b_{xy}) \quad (13)$$

397 where  $a_{xy}$  and  $b_{xy}$  are constants, which are, according to Morse et al. (2000), derived from  
 398  $NDVI(x, y)$  and  $GPS(x, y)$  data for known sample pixels representing the earlier classified land-  
 399 cover types, namely natural forest, desert, cotton, jujube, and cotton/jujube mixture.  
 400 Corresponding land-cover type  $Z_0$ 's are 0.45, 0.01, 0.18, 0.26, and 0.22 m, respectively; the  
 401 required average value over the entire LASAT model domain results in  $Z_0 = 0.22 \pm 0.158$  m.

402 Besides mechanical turbulence ( $Z_0$ ), atmospheric stability affects most the dispersion of trace  
 403 substances. For Milan oasis' atmospheric boundary layer, atmospheric stability has been cal-  
 404 culated according to the "solar radiation/delta T (SRDT)" method in 30 min intervals. This  
 405 method (c.f. Turner, 1994) is widely accepted because of its simplicity and its representative-  
 406 ness for atmospheric stability over open country and rural areas, like the Milan oasis domain.  
 407 Daytime stability classes are calculated from *in-situ* measurements of solar radiation and  
 408 horizontal wind speed (see Sect. 2.2.2).

409 Finally, 30 min means of all parameters and input variables of LASAT have been calculated.  
 410 Using these, about  $4 \times 10^6$  gridded data points of 3-D NO concentration have been calculated  
 411 for each time period considered in Section 3.2.

## 412 **2.2.8 Simulation of $SCD_{NO_2}$ and $VCD_{NO_2}$ by spatial integration of LASAT results**

413 There is only one tool to provide a robust relationship between biogenic soil NO emissions on  
 414 one hand and MAX-DOAS observed  $SCD$ 's and  $VCD$ 's on the other hand: the exact simula-  
 415 tion of the MAX-DOAS measurement through spatial integration of three dimensional NO  
 416 concentrations calculated by LASAT (followed by  $NO \rightarrow NO_2$  conversion). At a given  
 417 location of the MAX-DOAS measurement, integration must be performed from the height  
 418 where the MAX-DOAS instrument has been set-up ( $h_{MAXDOAS}$ ) to the end of the atmospheric  
 419 boundary layer ( $h_{ABL} = 1500$  m a.gr.) along two virtual light paths, (a) the vertical up path

420 (VCD), and (b) the slant path (SCD) according to the selected elevation angle of each MAX-  
 421 DOAS measurement.

422 Calculation of simulated VCD's for NO ( $VCD_{NO,sim}$ ) at the location of a MAX-DOAS  
 423 instrument is achieved as follows: (a) determination of the NO mass density ( $ng\ m^{-2}$ ) of the  
 424 vertical column between  $h_{MAXDOAS}$  and  $h_{ABL}$ ; this is obtained by adding NO concentrations  
 425 ( $ng\ m^{-3}$  in terms of mass of nitric oxide) of all LASAT cells in vertical direction over that  
 426  $30\ m \times 30\ m$  grid, which contains the location of the MAX-DOAS instrument, multiplied by  
 427 the height difference  $\Delta h = h_{ABL} - h_{MAXDOAS}$  (in m), (b) multiplying that NO mass density by  
 428 the ratio of Avogadro's number ( $6.02217 \times 10^{26}$  molecules  $kmol^{-1}$ ) and the molecular weight of  
 429 NO ( $30.0061 \times 10^{12}$   $ng\ kmol^{-1}$ ) delivers the desired value of  $VCD_{NO,sim}$  in units of molecules  
 430  $m^{-2}$  ( $\times 10^{-4}$ : molecules  $cm^{-2}$ ) at the location of the MAX-DOAS instrument. Calculation of  
 431 simulated SCD's for NO ( $SCD_{NO,sim}$ ) requires the determination of the 3-D light path through  
 432 the trace gas layered. Positioning of MAX-DOAS's telescope was always to the north, the  
 433 selected MAX-DOAS elevation angle  $\alpha$  and  $h_{ABL}$  deliver the length of the slant light path  
 434 ( $= h_{ABL}/\sin\alpha$ ). The desired  $SCD_{NO,sim}$  (in molecules  $m^{-2}$ ) results from the NO mass density of  
 435 the slant column multiplied by the length of the slant light path, where the NO mass density is  
 436 equivalent to the sum of all NO concentrations of those LASAT cells which are intersected by  
 437 the slant light path from the position of the MAX-DOAS instrument to  $h_{ABL}$ .

438 For conversion of  $VCD_{NO,sim}$  to  $VCD_{NO_2,sim}$  and  $SCD_{NO,sim}$  to  $SCD_{NO_2,sim}$  it is assumed, that  
 439 the photostationary state (PSS) of the triad NO,  $NO_2$ , and  $O_3$  is established in Milan oasis'  
 440 atmospheric boundary layer. According to Leighton (1961) this chemical equilibrium state is  
 441 due to fast photochemical reactions, namely  $NO + O_3 \rightarrow NO_2 + O_2$  and  $NO_2 + h\nu \rightarrow NO + O$ , from  
 442 which the so-called photostationary state  $NO_2$  concentration ( $NO_{2,PSS}$ ) can be derived as

$$443 \quad [NO_{2,PSS}] = \frac{[O_3][NO]k_1}{j(NO_2)} \quad (14)$$

444 where  $[O_3]$  is the ozone number density (molecules  $cm^{-3}$ ; calculated from *in-situ* measured  $O_3$   
 445 concentrations, see Sect. 2.2.2),  $[NO]$  is the NO number density,  $k_1$  is the reaction coefficient  
 446 of the  $NO + O_3 \rightarrow NO_2 + O_2$  reaction ( $cm^3\ molecules^{-1}\ s^{-1}$ ; Atkinson et al., 2004), and  $j(NO_2)$  is  
 447 the *in-situ* measured  $NO_2$  photolysis rate (in  $s^{-1}$ ; see Sect. 2.2.2). Finally,  $VCD_{NO_2,sim}$  and  
 448  $SCD_{NO_2,sim}$  are calculated from  $VCD_{NO,sim}$  and  $SCD_{NO,sim}$  by

$$449 \quad VCD_{NO_2,sim} = CF_0 \times VCD_{NO,sim} \quad \text{and} \quad SCD_{NO_2,sim} = CF_0 \times SCD_{NO,sim} \quad (15)$$

450 where the  $\text{NO} \rightarrow \text{NO}_2$  conversion factor is defined by  $CF_0 = [\text{O}_3] k_1 / j(\text{NO}_2)$ .

451 Since the  $\text{NO}-\text{NO}_2-\text{O}_3$  photochemical equilibrium could not be handled by LASAT's  
452 "chemical" algorithm, we decided to use measured data ( $\text{O}_3$  mixing ratio,  $\text{NO}_2$  photolysis rate,  
453 s. sect. 2.2.2) to convert the calculated 3D- $\text{NO}$  mixing ratio to the photo-stationary 3D- $\text{NO}_2$   
454 mixing ratio. For that, a constant vertical  $\text{O}_3$  mixing ratio (up to 1500 m a.gr.) is assumed over  
455 Milan oasis. This is justified by the fact, that particularly in arid and hyper-arid landscapes at  
456 mid-day conditions (maximum of insolation) the entire atmospheric boundary layer is  
457 intensively mixed, which is due to extensive convective heating of the surface by the sun  
458 which produces powerful buoyant thermals that establish the so-called mixing layer.  
459 Consequently an uniform vertical mixing ratio is expected for trace gases with chemical  
460 lifetimes greater than the exchange time of the atmospheric boundary layer. (c.f. Husar et al.  
461 1978, Stull 1988). This assumption is valid for ozone. Vertically constant  $\text{O}_3$  mixing ratio  
462 has been reported for the atmospheric boundary layer over semi-arid southern Africa  
463 (Meixner et al., 1993). Concerning the vertical distribution of  $j(\text{NO}_2)$  it is obvious, that the  
464 downward component of the actinic flux increases with increasing elevation due to the  
465 decreasing optical thickness of the scattering air masses. However, the altitude effect on the  
466 actinic flux in the first kilometer of the troposphere is typically very small. Trebs et al. (2009)  
467 used the Tropospheric Ultraviolet Visible model to calculate the typical vertical change of the  
468 actinic flux and found a vertical gradient of 1.1%/km. Consequently, our calculations of the  
469  $\text{NO}$  to  $\text{NO}_2$  conversion in the boundary-layer over Milan oasis (1500 m a.gr.) have not  
470 considered any potential vertical change of the  $j(\text{NO}_2)$  values measured at ground level.  
471 Nevertheless, for the case of our measurements the locally enhanced  $\text{NO}$  values caused by the  
472 soil emissions have a small but systematic effect on the ozone concentration, and thus also on  
473 the Leighton ratio: Close to the surface (below about 50m) the  $\text{NO}$  concentrations can be  
474 quite large, with maximum values up to about 10 ppb. Consequently, the ozone concentration  
475 will be reduced due to the reaction with  $\text{NO}$  by up to about 10 ppb. This means that the  
476 Leighton ratio will be reduced by up to about 25%. Although the reduction of the ozone  
477 mixing ratio will be partly compensated by mixing with air from higher altitudes, the  
478 simulated  $\text{NO}_2$  mixing ratios might overestimate the true  $\text{NO}_2$  mixing ratios by up to about  
479 25%. Probably the true overestimation for our measurements is much smaller because the  
480 typical  $\text{NO}$  mixing ratio within the lowest 100m is much lower than 10 ppb.

### 481 **3 Results and Discussion**

### 482 **3.1 Land-cover type specific net potential NO fluxes**

483 Net potential NO fluxes (as functions of soil temperature and moisture) have been determined  
484 by incubation of samples which have been taken from the top-soil of Milan oasis' major land-  
485 cover types, i.e. natural forest, desert, cotton, jujube, and cotton/ujube mixture (see Sect.  
486 2.2.4). Figure 2 shows the laboratory derived net potential NO flux,  $F_{NO}$  from soils of the  
487 most contrasting land-cover types of Milan oasis (irrigated & fertilized fields of cotton,  
488 jujube, cotton/ujube mixture, and desert).

489 Net potential NO fluxes of the natural forest land-cover type are not shown, because  
490 laboratory incubation measurements have shown that there is no significant NO release from  
491 these soils, most likely due to its high electrical conductivity (salt content). Optimum  
492 gravimetric soil water contents (i.e., where the maximum of  $F_{NO}$  is observed) for desert,  
493 managed cotton, and managed jujube soils have one in common, very low values of  $\theta_{g,opt}$   
494 (0.009–0.017) for soil temperatures of 50°C. During the vegetation period (April –  
495 September), soil temperatures of >40°C are easily reached for the soils of Milan oasis,  
496 particularly for the desert soils. While the nature of all Milan oasis' soils is arid/hyper-arid,  
497 maximum net potential NO fluxes are 7600, 63, 270, and 98 ng m<sup>-2</sup> s<sup>-1</sup> (in terms of mass of  
498 nitric oxide) for cotton, jujube, jujube/cotton mixture, and desert soils, respectively.

### 499 **3.2 Land-cover types of Milan oasis and actual NO fluxes**

500 As mentioned in Section 2.2.5, land-cover classification and actual distribution of Milan  
501 oasis' fields have been identified from satellite images (Quickbird, Landsat ETM+). The 2011  
502 distribution of fields and the corresponding land-cover is shown in Figure 3.

503 The dominant crop was cotton, representing 18% (64 km<sup>2</sup>) of the total field area of Milan  
504 oasis (ujube 7%, 28 km<sup>2</sup>), cotton/ujube mixture 0.89 % (3 km<sup>2</sup>), natural forest 18% (64 km<sup>2</sup>),  
505 residential area 1.62% (5.5 km<sup>2</sup>) and desert 52% (174 km<sup>2</sup>). Land-cover specific, actual NO  
506 fluxes (30 min means) from cotton, jujube, cotton/ujube, and desert soils were calculated  
507 from corresponding laboratory derived net potential NO fluxes, land-type specific soil  
508 moisture and soil temperature data (see Sect. 2.2.6). These NO fluxes (ng m<sup>-2</sup> s<sup>-1</sup>, in terms of  
509 mass of nitric oxide) were then assigned to each individual source unit (i.e. to each of the  
510 2500 polygons of Milan oasis' domain).

511 For the period 03 to 24 June, 2011, land-cover specific, actual NO fluxes were calculated  
512 according to eq.(10) for cotton, jujube, cotton/ujube, and desert soils from corresponding  
513 laboratory derived net potential NO fluxes. As input we used land-type specific, measured

514 soil temperature data as well as land-type specific soil moisture data (so-called “wilting  
515 points”, s. Sect. 2.2.3). The calculated NO fluxes are shown in Fig. 4 as median diel variation  
516 (for the entire period of 03 to 24 June, 2011). Since NO fluxes from Milan cotton fields  
517 dominate the total soil biogenic NO emission of the oasis, corresponding medians and  
518 quartiles are shown in Fig. 4, while – for the sake of clarity – for jujube, cotton/jujube, and  
519 desert only medians are given. Since land-type specific “wilting points” are constant, diel  
520 variations of actual NO fluxes mirror directly those of corresponding soil temperatures,  
521 showing the daily minimum around 06:00 local time for all four major land-cover types. The  
522 maximum of the actual NO-flux, however, is around 13:00 (local time) for jujube,  
523 cotton/jujube, and desert soils, and 15:00 local time for cotton. This is due to the growth of  
524 the cotton plants: while at the beginning of the experimental period the bare soil surface was  
525 nearly 100% exposed to insolation, the growing cotton canopy has shaded great parts of the  
526 soil surface towards the end of the experimental period. This is also reflected by the skewed  
527 distribution of actual NO-fluxes from cotton covered soil, indicated by the daytime non-  
528 symmetric inter-quartile range (= upper quartile – lower quartile). As shown in sect. 3.5,  
529 actual NO-flux data of 09 June, 2011 (08:30-14:30 local time) were used for the comparison  
530 of LASAT and MAX-DOAS results. During this particular day (within the first week of the  
531 experimental period), the derived flux for “land-cover cotton” ranged from 15–64  $\text{ng m}^{-2}\text{s}^{-1}$   
532 (in terms of mass of NO), those for jujube, cotton/jujube, and desert land-covers ranged from  
533 11–13, 6–16, and 6–17  $\text{ng m}^{-2}\text{s}^{-1}$ , respectively. These actual NO fluxes were then assigned to  
534 each individual source unit (i.e. to each of the 2500 polygons of Milan oasis’ domain). The  
535 soil biogenic NO emission from all cotton fields between 08:30 and 14:30 was estimated to  
536 28.7 kg (in terms of mass of NO), equivalent to 76% of the total soil biogenic NO emission of  
537 the entire Milan oasis within 6 hours.

### 538 3.3 Vertical NO<sub>2</sub> column densities by MAX-DOAS

539 We performed 32 individual MAX-DOAS measurements within 21 days of the 2011 field  
540 campaign to examine the spatial variation between the observed sites. In Fig. 5, all observed  
541 vertical NO<sub>2</sub> column densities (in molecules  $\text{cm}^{-2}$ ) observed at sites (1) - (4) of Milan oasis are  
542 shown in polar coordinates with reference to corresponding wind directions measured *in-situ*  
543 at the individual sites.

544 Wind speeds (30 min means) ranged between 1.5 and 7.7  $\text{m s}^{-1}$  and wind direction was mostly  
545 (78%) from the northern quadrants (59%, 9%, 13%, and 19% from NE, SE, SW, and NE  
546 quadrants, respectively). As expected, highest VCDs ( $10^{15} - 10^{16}$  molecules  $\text{cm}^{-2}$ ) were

547 observed at site (4) (Milan oasis center), regardless of wind direction. When the wind  
548 direction is from the NE quadrant, site (3) (jujube fields) is down-wind of Milan oasis (see  
549 Fig.1); then its VCDs are as high as those obtained in the oasis' center ( $5 - 7 \times 10^{15}$  molecules  
550  $\text{cm}^{-2}$ ). The few VCD data points of  $1 \times 10^{15}$  molecules  $\text{cm}^{-2}$  at the jujube site, attributed to  
551 winds from SE and SW quadrants, are mainly due to NO emissions from traffic on the  
552 National Road 315 which passes the southern margins of Milan oasis. Lowest VCDs  
553 ( $3 \times 10^{13} - 3 \times 10^{14}$  molecules  $\text{cm}^{-2}$ ) have been observed at site (1) (natural forest) and site (2)  
554 (desert). Alone from these spatially resolved VCD observations in the Milan oasis' domain,  
555 the increase of VCD due to the oasis itself can be estimated in the order of at least one order  
556 of magnitude.

557 Fortunately, we have been able to perform simultaneous measurements with two MAX-  
558 DOAS instruments at sites (1) and (3) on 09 and 13 June, 2011. Since winds (approx.  $3 \text{ m s}^{-1}$ )  
559 were from the NE quadrant during these two days, site (1) has been up-wind, and site (3)  
560 downwind of Milan oasis. Corresponding VCD results are shown in Figure 6.  $\text{NO}_2$  VCDs at  
561 the downwind site exceeded those at the upwind site by factors 5 – 9. This difference between  
562 downwind and upwind MAXDOAS signals is considered to be a direct measure for the areal  
563 increase of ambient  $\text{NO}_2$  concentration. In the absence of anthropogenic  $\text{NO}_x$  sources (see  
564 Sect. 2.1), this provides first evidence for the considerable impact of the biogenic NO emissi-  
565 ons from the fields of Milan oasis.

### 566 3.4 3-D distribution of ambient NO-concentration

567 The LASAT model has to be used to calculate the dispersion of soil emitted NO into the at-  
568 mospheric boundary layer over Milan oasis. An example for the resulting distribution of NO  
569 concentration in the first four vertical layers of LASAT (0-3, 3-5, 5-10, and 10-20 m) is  
570 shown in Figure 7 (09 June, 2011; 11:30-13:00 local time). The shown results are the mean of  
571 three LASAT model runs, since a new LASAT calculation of 3-D distribution of NO  
572 concentration is started for every set of meteorological parameters which are provided every  
573 30 min from means of the *in-situ* measured meteorological quantities (see Sect. 2.2.2). During  
574 11:30-13:00, mean wind direction was  $15^\circ$ ,  $38^\circ$ , and  $50^\circ$ , wind speed was rather constant  
575 ( $2.60 - 2.67 \text{ m s}^{-1}$ ), and atmospheric stability class has been generally neutral (3.2).

576 By comparing the NO ambient concentrations, particularly in the first vertical LASAT layer  
577 (0–3 m) of oasis area with the surrounding desert, it becomes obvious that the great differ-  
578 ences of ambient NO concentrations mirror the corresponding differences of actual soil NO  
579 fluxes from each source-unit; within this layer calculated mean NO concentrations are 13, 12,

580 10, and  $1 \text{ ng m}^{-3}$  (in terms of mass of nitric oxide; or 10.6, 9.8, 8.2, and 0.8 ppb) for the oasis  
581 centre, jujube fields, cotton/jujube mixture, and desert, respectively. The value at the oasis  
582 center exceeds those over desert by more than an order of magnitude, similar as the  
583 corresponding VCD values (see above). As expected under the prevailing conditions of well  
584 developed atmospheric turbulence, NO concentrations rapidly decreases with height (see  
585 panels “0–3 m”, “3–5 m”, “5–10 m” in Fig. 7), and with prevailing northerly winds, the NO  
586 concentration centre shifting southwards with increasing altitude.

### 587 3.5 Simulated SCDs and VCDs vs. SCDs and VCDs by MAX-DOAS

588 For those periods where simultaneous “upwind” and “downwind” MAX-DOAS  
589 measurements have been performed (09 and 13 June, 2011), corresponding  $\text{SCD}_{\text{sim}}$  and  
590  $\text{VCD}_{\text{sim}}$  have been simulated by suitable vertical integration (see Sect. 2.2.8) of LASAT-  
591 calculated 3-D NO concentrations, followed by  $\text{NO} \rightarrow \text{NO}_2$  conversion (based on  
592 photostationary state assumption of Milan oasis’ atmospheric boundary layer). Since  $\text{SCD}_{\text{sim}}$   
593 and  $\text{VCD}_{\text{sim}}$  represent only that part of true SCDs and VCDs of  $\text{NO}_2$ , which are due to the  
594 contribution of the oasis’ soil NO emissions,  $\text{SCD}_{\text{sim}}$  and  $\text{VCD}_{\text{sim}}$  are compared to the  
595 difference of those SCDs and VCDs which have been simultaneously measured by two  
596 MAX-DOAS instruments at corresponding “downwind” and “upwind” sites (see Fig. 8). For  
597 elevation angles of  $2^\circ$  and  $4^\circ$ ,  $\text{SCD}_{\text{sim}}$  and  $\Delta\text{SCD} = \text{SCD}_{\text{down}} - \text{SCD}_{\text{up}}$  are shown in Figure 8a.  
598 In Figure 8b,  $\text{VCD}_{\text{sim}}$  and  $\Delta\text{VCD} = \text{VCD}_{\text{down}} - \text{VCD}_{\text{up}}$  are shown for  $15^\circ$  elevation.

599 Here it should be noted that in principle the accuracy of the geometric approximation is  
600 higher for the high elevation angles than for the lower elevation angles. However, for the  
601 specific cases studied here, this is not the case. First, close to the sources, the height of the  
602 layer with elevated  $\text{NO}_2$  is quite low (in our case the bulk of  $\text{NO}_2$  is located below 100 m).  
603 Second, also the aerosol load is usually very low. Thus the probability of scattering events  
604 inside the layer of enhanced  $\text{NO}_2$  is very low, and consequently the accuracy of the geometric  
605 approximation is relatively high. To further quantify the associated uncertainties, we  
606 performed radiative transfer simulations and found that the deviations from the geometric  
607 approximation are similar for the different elevation angles (about 5% for  $2^\circ$ , 3% for  $4^\circ$  and  
608 3% for  $15^\circ$ ). However, because of the shorter light paths through the  $\text{NO}_2$  layer, the relative  
609 error caused by the uncertainty of the spectral analysis is higher than for the low elevation  
610 angles. Thus for the case of our measurements, we indeed expect lower uncertainties for the  
611 low elevation angles.

612 Since soil NO emission data used in the LASAT dispersion model were calculated from land-  
613 cover type specific potential net NO fluxes, which in turn were derived from laboratory  
614 incubation experiments on corresponding soil samples, the results in Figure 8 are also  
615 considered as an excellent quality assurance of the chosen up-scaling of laboratory results to  
616 the oasis scale. There is remarkable good agreement between measured and simulated data.  
617 However, the actual NO emissions (irrespective of the land-cover type) have their maximum  
618 in the early afternoon (s. Fig. 4), while the highest height-integrated NO<sub>2</sub> concentrations as  
619 simulated by LASAT (on the basis of the actual NO emissions) are in the morning (08:30–  
620 10:00), followed by rather constant values for the remainder of the day (s. Fig. 8). The apparent  
621 discrepancy between both diurnal variations can be simply explained by the diurnal variation  
622 of the wind direction and the specific viewing geometry of the MAX-DOAS instrument. The  
623 MAX-DOAS instrument was located at the south-west corner of the oasis, and the  
624 observations at zenith and low elevation angles probed air masses located at different  
625 locations across the oasis. The wind direction was from north-east in the morning and turned  
626 to north-west in the afternoon. Hence, air masses of lower concentration crossed the viewing  
627 directions in the afternoon compared to those in the morning. This explains that in spite of the  
628 larger NO<sub>x</sub> emissions smaller column densities have been observed in the afternoon. The  
629 apparent discrepancy of the diurnal cycles of NO emissions and measured NO<sub>2</sub> column  
630 densities indicates the importance to exactly consider the 3-dimensional NO<sub>2</sub> distribution (due  
631 to the soil-emitted NO) for the comparison of the model results with MAX-DOAS  
632 observations.

633 The Figure 8b shows that the LASAT simulations overestimate slightly the true NO<sub>2</sub> VCD.  
634 The both measured and simulated NO<sub>2</sub> VSDs have with an average root mean square (RMS)  
635 error between the measured and simulated values of approx. 5-15%. However, the  
636 overestimation of LASAT simulation is well suited to the fact that in reality a little less NO  
637 can be converted to the NO<sub>2</sub> because of lower ozone concentration at the surface.

#### 638 **4 Conclusion**

639 This study has been focused on the following activities: (1) representative soil sampling from  
640 the uppermost soil layer (< 0.05 m) of all land-cover type units (natural forest, cotton fields,  
641 jujube fields, cotton/jujube mixture, desert) of Milan oasis (Xinjiang, NW China), (2) labora-  
642 tory incubation experiments (dynamic chamber system) to characterize the biogenic NO emis-  
643 sion from these soil samples in form of net potential NO fluxes as function of soil moisture  
644 and soil temperature, (3) determination of the actual size, areal distribution, and land-cover

645 type of Milan oasis' field units from satellite remote sensing information, (4) field measure-  
646 ments of slant (SCD) and vertical (VCD) NO<sub>2</sub> column densities (by MAX-DOAS) and  
647 additional quantities (soil moisture, soil temperature, ozone concentration, NO<sub>2</sub> photolysis  
648 rate, meteorological parameters) during an extended field campaign of 4 weeks at Milan oasis,  
649 (5) using data from (2), (3) and (4): calculation of Milan oasis' 2D distribution of actual, land-  
650 cover specific NO fluxes, (6) calculation of 3-D NO concentrations in Milan oasis' atmosphe-  
651 ric boundary layer originating from the dispersion of biogenic NO soil emissions determined  
652 by (5) with help of the Lagrangian dispersion model LASAT, (7) simulation of SCDs and  
653 VCDs by suitable vertical integration of calculated 3-D NO concentrations followed by  
654 suitable NO→NO<sub>2</sub> conversion factors derived from *in-situ* measurements, (8) comparison of  
655 measured and simulated SCDs and VCDs.

656 Results of the laboratory derived NO fluxes have shown that the extensively managed (ferti-  
657 lized and efficiently irrigated) cotton fields of Milan oasis release large amounts of soil bio-  
658 genic NO; NO fluxes range between 10–30 ng m<sup>-2</sup> s<sup>-1</sup> (in terms of mass of N), that is approx.  
659 5–10 times more than from a typical central European wheat field (Yamulki et al. 1995; Stohl  
660 et al. 1996).

661 Applying two MAX-DOAS instruments, simultaneous measurements have been performed at  
662 upwind and downwind sites of Milan oasis. Downwind site VCDs exceeded those from the  
663 upwind site by factors 5 – 9. Differences of VCD and SSC (“downwind” minus “upwind”) are  
664 a direct measure for the areal increase of ambient NO<sub>2</sub> concentration caused by the oasis  
665 itself. The measured differences of VCDs and SCDs were compared with the simulated VCDs  
666 and SCDs and excellent agreement was found.

667 This agreement is considered as the first successful attempt to prove the validity of the chosen  
668 approach to up-scale laboratory derived biogenic NO fluxes to ecosystem level field con-  
669 ditions, i.e. from the spatial scale of a soil sample (cm<sup>2</sup>) to field size (ha), and from field size  
670 (ha) to the size of an entire (agro-) ecosystem (km<sup>2</sup>). Furthermore, in the absence of anthropo-  
671 genic NO sources of Milan oasis (hydropower energy, battery powered trikes), it is obvious,  
672 that the areal increase of ambient NO<sub>2</sub> concentration in the atmospheric boundary layer of the  
673 isolated (in terms of NO<sub>2</sub> advection) Milan oasis is entirely due to biogenic NO emission from  
674 the arid/hyper-arid soils of the oasis itself. Extensive agricultural management of Milan oasis'  
675 crop fields (fertilization (350–600 kg N ha<sup>-1</sup>a<sup>-1</sup>) and effective irrigation of cotton and jujube  
676 fields) obviously provides considerable contribution of biogenic NO<sub>x</sub> (NO+NO<sub>2</sub>) from  
677 arid/hyper-arid soils of the Taklimakan desert to the local tropospheric NO<sub>x</sub> budget.

678 About 80% of the Chinese cotton production originates from the 3000 km long belt of oases  
679 surrounding Taklimakan Desert ( $1.65 \times 10^6 \text{ km}^2$ ) in Xinjiang (NW-China); cotton cultivated  
680 land area in Xinjiang occupies the first place of entire China. Since 1955, Xinjiang's output of  
681 cotton increased 294 times (Lei et al., 2005). Fast economic growth in the region (+11% GDP  
682  $\text{a}^{-1}$ ), inevitably accompanied by large anthropogenic  $\text{NO}_x$  emissions (traffic, energy producti-  
683 on), may be countervailed or even exceeded by the “hotspot” character of Xinjiang’s oases,  
684 namely by soil biogenic NO emissions from agriculturally dominated oases. Most likely, they  
685 will contribute most to the regional tropospheric  $\text{NO}_x$  budget. This is all the more likely,  
686 given the continued intensification of oasis agriculture around the Taklimakan desert which  
687 will be accompanied by corresponding land use change (desert→dryland farming with  
688 irrigation) in the coming decades.

### 689 **Acknowledgements**

690 This work was funded through the German Research Foundation (DFG) project “DEQNO –  
691 Desert Encroachment in Central Asia – Quantification of soil biogenic Nitric Oxide” (DFG-  
692 MA 4798/1-1), the Max Planck Society (MPG), and the Max Planck Graduate Centre with  
693 Johannes Gutenberg-University Mainz (MPGC). The authors like to thank Guozheng Song,  
694 Günter Schebeske, Achim Zipka, Yanhong Li, Fanxia Wang, Aixia Yang, Sijun Luo, and  
695 Zhilin Zhu for their field assistance and their substantial support before, during, and after the  
696 DEQNO 2011 campaign. We also thank Reza Shaiganfar and Steffen Beirle for their supports  
697 during the pre-preparation of MAX-DOAS instrument.

698

699

700

701 **References:**

- 702 Ashuri, F.A.: Der Austausch von Stickstoffmonoxid zwischen Boden und Atmosphäre unter  
703 besonderer Berücksichtigung des Bodenwassergehaltes, Einfluss kulturlandschaftlicher  
704 Verhältnisse auf den Umsatz eines Spurengases. Ph.D. thesis, Johannes Gutenberg  
705 University Mainz, Mainz, Germany, 1–169, 2009.
- 706 Atkinson, R., Baulch, D.L., Cox, R.A., Crowley, J.N., Hampson, R.F., Hynes, R.G., Jenkin,  
707 M.E., Rossi, M.J., Troe, J.: Evaluated kinetic and photochemical data for atmospheric  
708 chemistry: Volume I - Gas phase reactions of Ox, HOx, NOx and SOx species, *Atmos.*  
709 *Chem. Phys.*, 4, 1461–1738, 2004.
- 710 Bargsten, A., Falge, E., Pritsch, K., Huwe, B., Meixner, F.X.: Laboratory measurements of  
711 nitric oxide release from forest soil with a thick organic layer under different understory  
712 types, *Biogeosciences*, 7, 1425–1441, 2010.
- 713 Behrendt, T., Veres, P.R., Ashuri, F., Song, G., Flanz, M., Mamtimin, B., Bruse, M.,  
714 Williams, J., Meixner, F.X.: Characterisation of NO production and consumption: new in-  
715 sights by an improved laboratory dynamic chamber technique, *Biogeosciences Discuss.*,  
716 11, 1187–1275, 2014.
- 717 Beirle, S., Platt, U. Wenig, M. and Wagner, T.: Highly resolved global distribution of  
718 tropospheric NO<sub>2</sub> using GOME narrow swath mode data, *Atmos. Chem. Phys.*, 4, 1913-  
719 1924, 2004.
- 720 Bogumil, K., Orphal, J., Homann, T., Voigt, S., Spietz, P., Fleischmann, O.C., Vogel, A.,  
721 Hartmann, A., Kromminga, H., Bovensmann, H., Frerick, J., Burrows, J.P.: Measurements  
722 of molecular absorption spectra with the SCIAMACHY pre-flight model: instrument  
723 characterization and reference data for atmospheric remote-sensing in the 230–2380 nm  
724 region, *Journal of Photochemistry and Photobiology A-chemistry*, 157(2), 167-184, 2003.
- 725 Brinksma, E. J., Pinardi, G., Volten, H., Braak, R., Richter, A., Schoenhardt, A., Van  
726 Roozendaal, M., Fayt, C., Hermans, C., Dirksen, R. J., Vlemmix, T., Berkhout, A.J.C.,  
727 Swart, D.P. J., Oetjen, H., Wittrock, F., Wagner, T., Ibrahim, O. W., Leeuw, G. de.,  
728 Moerman, M., Curier, R. L., Celarier, E. A., Cede, A., Knap, W. H., Veefkind, J. P.,  
729 Eskes, H. J., Allaart, M., Rothe, R., Piters, A. J. M., Levelt, P. F.: The 2005 and 2006  
730 DANDELIONS NO<sub>2</sub> and aerosol intercomparison campaigns, *Journal of Geophysical*  
731 *Research*, Vol. 113, 1-18, 2008.
- 732 Chameides, W. L., Fehsenfeld, F., Rodgers, M. O., Cardelino, C., Martinez, J., Parrish, D.,  
733 Lonneman, W., Lawson, D. R., Rasmussen, R. A., Zimmerman, P., Greenberg, J.,  
734 Middleton, P., Wang, T.: Ozone precursor relationships in the ambient atmosphere, *Journal*  
735 *of Geophysical Research*, 92, 6037-6055, 1992.
- 736 Chander, G. and Markham, B.: Revised Landsat-5 TM radiometric calibration procedures and  
737 postcalibration dynamic ranges, *IEEE Transactions on Geoscience and Remote Sensing*, 41  
738 (11), 2674-2677, 2003.
- 739 Conrad, R.: Soil Microorganisms as controllers of atmospheric trace gases (H<sub>2</sub>, CO, CH<sub>4</sub>,  
740 COS, N<sub>2</sub>O and NO), *Microbiological Reviews.*, 60 (4), 609–640, 1996.
- 741 Crutzen, P. J. (1987): Role of the tropics in atmospheric chemistry, in: *The Geophysiology of*  
742 *Amazonia*, Dickinson, R.E. (ed.), pp. 107-132, 1987, John Wiley & Sons, New York.
- 743 Davidson, E. A., Kingerlee, W.: A global inventory of nitric oxide emissions from soils,  
744 *Nutrient Cycling in Agroecosystems*, 48, 37–50, 1997.
- 745 Denman, K.L., Brasseur, G.P., Chidthaisong, A., Ciais, P., Cox, P.M., Dickinson, R.E.,  
746 Hauglustaine, D., Heinze, C., Holland, E.A., Jacob, D.J., Lohmann, U., Ramachandran,  
747 S., Da Silva Dias, P.L., Wofsy, S.C., Zhang, X.: Couplings between changes in the climate  
748 system and biogeochemistry, in *Climate Change 2007: The physical science basis.*  
749 contribution of working group 1 to the fourth assessment report of the Intergovernmental

750 Panel on Climate Change, edited by Solomon, S., Qin, D., Manning, M., Chen, Z.,  
751 Marquis, M., Averyt, K.B., Tignor, M., Miller, H.L., Cambridge University Press,  
752 Cambridge, 499-588, 2007.

753 Feig, G.T.: Soil Biogenic Emissions of Nitric Oxide from Arid and Semi-Arid Ecosystems,  
754 PhD thesis, Johannes Gutenberg University Mainz, Mainz, Germany, 1–222, 2009.

755 Feig, G.T., Mamtimin, B., Meixner, F. X.: Soil biogenic emissions of nitric oxide from a  
756 semiarid savanna in South Africa, *Biogeosciences*, 5, 1723–1738, 2008a.

757 Feig, G.T., Mamtimin, B., Meixner, F. X.: Use of laboratory and remote sensing techniques to  
758 estimate vegetation patch scale emissions of nitric oxide from an arid Kalahari savanna,  
759 *Biogeosciences Discuss.*, 5, 4621–4680, 2008b.

760 Galbally, I.E., Johansson, C.: A model relating laboratory measurements of rates of nitric  
761 oxide production and field measurements of nitric oxide emissions from soils, *Journal of*  
762 *Geophysical Research*, 94, 6473- 6480, 1989.

763 Ganzeveld, L., Eerdeken, G., Feig, G.T., Fischer, H., Harder, H., Königstedt, R., Kubistin,  
764 D., Martinez, M., Meixner, F.X., Scheeren, B., Williams, J., Lelieveld, J.: Boundary layer  
765 exchanges of volatile organic compounds, nitrogen oxides and ozone during the GABRIEL  
766 campaign, *Atmospheric Chemistry and Physics*, 8, 6223-6243, 2008.

767 Gelfand, I., Feig, G., Meixner, F.X., Yakir, D.: Afforestation of semi-arid shrubland reduces  
768 biogenic NO emission from soil, *Soil Biology and Biochemistry* 41, 1561–1570, 2009.

769 Harrison, P., Pearce F.: Deserts and Drylands, AAAS Atlas of Population and Environment,  
770 pp. 131-134, 2000. University of California Press, Berkeley, USA.

771 Hartge, H., Horn, R.: Die physikalische Untersuchung von Böden: Praxis Messmethoden  
772 Auswertung. Schweizerbart-sche Verlagsbuchhandlung, Stuttgart, 1-178, 2009.

773 Hermans, C., Vandeale, A.C., Carleer, M., Fally, S., Colin, R., Jenouvrier, A., Coquart, B.,  
774 Merienne, M. F.: Absorption Cross-Sections of Atmospheric Constituents, NO<sub>2</sub>, O<sub>2</sub>, and  
775 H<sub>2</sub>O, *Environ. Sci. Pollut. Res.*, 6, 151-158, 1999.

776 Hönninger, G. and Platt, U.: The Role of BrO and its Vertical Distribution during Surface  
777 Ozone Depletion at Alert, *Atmos. Environ.*, 36, 2481–2489, 2002.

778 Hönninger, G., von Friedeburg, C., and Platt, U.: Multi Axis Differential Optical Absorption  
779 Spectroscopy (MAX-DOAS), *Atmos. Chem. Phys.*, 4, 231–254, 2004.

780 Husar, R.B., Patterson, D.E., Husar, J.D., Gillani, N.V., Wilson Jr., W.E. (1978), Sulfur  
781 budget of a power plant plume, *Atmospheric Environment*, 12 (1-3), 549-568.

782 IVU Umwelt GmbH: LASarc – GIS integration of LASAT, Environmental Planning and  
783 Information Systems, Freiburg, Germany, 2012.

784 Janicke Consulting: Dispersion model LASAT, Version 3.2, Reference Book. Janicke  
785 Consulting, Überlingen, Germany, 239 p, 2011.

786 Kargas, G., Ntoulas, N., Nektarios, P.A.: Soil texture and salinity effects on calibration of  
787 TDR300 dielectric moisture sensor. *Soil Research*, 51 (4), 330-340, 2013.

788 Kirkman, G.A., Yang, W.X., Meixner, F.X.: Biogenic nitric oxide emissions upscaling: An  
789 approach for Zimbabwe, *Global Biogeochem. Cycles*, 15, 1005–1020, 2001.

790 Koeppen, W.: Grundriss der Klimakunde. Gruyter Verlag, Berlin/Leipzig, Germany, 388 p,  
791 1931.

792 Kottke, M., Grieser, J., Beck, C., Rudolf, B. and Rubel, F.: World Map of the Köppen-Geiger  
793 climate classification Updated, *Meteorologische Zeitschrift*, 15 (3), 259-263, 2006.

794 Kurucz, R. L., Furenlid, I., Brault, J., Testerman, L.: Solar Flux Atlas from 296 nm to 1300  
795 nm, National Solar Observatory Atlas No. 1, 1984. Office of University publisher, Harvard  
796 University, Cambridge.

- 797 Lei, J., Zhang, X. L.: Structural Adjustment of Oasis Agriculture in Xinjiang, Chinese Journal  
798 of Population, Resources and Environment, 3 (3), 29-33, 2005.
- 799 Leighton, P. A.: Photochemistry of Air Pollution, Academic Press, New York and London,  
800 300 p, 1961.
- 801 Leue, C., Wenig, M., Wagner, T., Platt, U., Jähne, B.: Quantitative analysis of NO<sub>x</sub> emissions  
802 from GOME satellite image sequences, J. Geophys. Res., 106, 5493-5505, 2001.
- 803 Ludwig, J., Meixner, F.X., Vogel, B., Förstner, J.: Processes, influencing factors, and  
804 modelling of nitric oxide surface exchange—an overview, Biogeochemistry, 52 (3), 225-  
805 257, 2001.
- 806 Mayer, J.-C., Bargsten, A., Rummel, U., Meixner, F.X., Foken, T.: Distributed modified  
807 bowen ratio method for surface layer fluxes of reactive and non-reactive trace gases,  
808 Agricultural and Forest Meteorology, 151, 655-668, 2011.
- 809 Meixner, F.X., Ajavon, A.-L., Helas, G., Scharffe, D., Zenker, T., Harris, G.W., Andreae,  
810 M.O. (1993), Vertical distribution of ozone over southern Africa: Airborne measurements  
811 during SAFARI-92, AGU Fall Meeting, San Francisco, U.S.A.
- 812 Meixner, F.X., Yang, W.X.: Biogenic emissions of nitric oxide and nitrous oxide from arid  
813 and semiarid land, in: Dryland Ecohydrology, edited by: D'Odorico, P. and Porporat, A.,  
814 Springer, Dordrecht, the Netherlands, 233–255, 2006.
- 815 Morse, A., Tasumi, M., Allen, R. G., and Kramber, W. J. (2000): Application of the SEBAL  
816 Methodology for Estimating Consumptive Use of Water and Streamflow Depletion in the  
817 Bear River Basin of Idaho through Remote Sensing, Final report submitted to The  
818 Raytheon Systems Company, Earth Observation System Data and Information System  
819 Project, Boise, USA, 107 pp., 2000.
- 820 Otter, L.B., Yang, W.X., Scholes, M.C., Meixner, F. X.: Nitric Oxide emissions from a  
821 southern African Savannah, J. Geophys. Res., 104, 18471–18485, 1999.
- 822 Perumal, K. and Bhaskaran, R.: Supervised classification performance of multispectral  
823 images. Journal of Computing, 2-2, 124-129, 2010.
- 824 Platt, U. and Stutz, J.: Differential Optical Absorption Spectroscopy: Principles and  
825 Applications, Springer, Berlin, Heidelberg, Germany, 135–377, 2008.
- 826 Rothman, L.S., Jacquemart, D., Barbe, A., Chris Benner, D., Birk, M., Brown, L.R., Carleer,  
827 M.R., Chackerian Jr, C., Chance, K., Coudert, L.H., Dana, V., Devi, V.M., Flaud, J.-M.,  
828 Gamache, R.R., Goldman, A., Hartmann, J.-H., Jucks, K.W., Maki, A.G., Mandin, J.-Y.,  
829 Massie, S.T., Orphal, J., Perrin, A., Rinsland, C.P., Smith, M.A.H., Tennyson, J.,  
830 Tolchenov, R.N., Toth, R.A., Vander Auwera, J., Varanasi, P., Wagner, G.: The HITRAN  
831 2004 molecular spectroscopic database, Journal of Quantitative Spectroscopy & Radiative  
832 Transfer, 96, 139-204, 2005.
- 833 Rudolph, J., Conrad, R.: Flux between soil and atmosphere, vertical concentration profiles in  
834 soil, and turnover of nitric oxide: 2. Experiments with naturally layered soil cores, Journal  
835 of Atmospheric Chemistry, 23, 275-300, 1996.
- 836 Rudolph, J., Rothfuss, F., Conrad, R.: Flux between soil and atmosphere, vertical  
837 concentration profiles in soil, and turnover of nitric oxide: 1. Measurements on a model  
838 soil core, Journal of Atmospheric Chemistry, 23, 253–273, 1996.
- 839 Richter, A., Burrows, J.P.: Tropospheric NO<sub>2</sub> from GOME Measurements, Adv. Space Res.,  
840 29(11), 1673-1683, 2002.
- 841 Simiu, E., Scanlan, R.H.: Wind Effects on Structures: Fundamentals and Applications to  
842 Design, Third Edition, John Wiley & Sons, New York, USA, 704 p., 1996.

843 Sinreich, R., Frieß, U., Wagner, T., Platt, U.: Multi axis differential optical absorption  
844 spectroscopy (MAX-DOAS) of gas and aerosol distributions, *Faraday Discuss.*, 130, 153–  
845 164, doi:10.1039/b419274p, 2005.

846 Solomon, S., Schmeltekopf, A. L., Sanders, R. W.: On the interpretation of zenith sky  
847 absorption measurements, *J. Geophys. Res.*, 92, 8311–8319, 1987.

848 Stohl, A., Williams, E., Wotawa, G. and Kolb, H.K.: A European Inventory of Soil Nitric  
849 Oxide Emissions and the Effect of these Emissions on the Photochemical Formation of  
850 Ozone, *Atmospheric Environment*, 30 (22), 3741–3755, 1996.

851 Stull, R.B. (1988), *An Introduction to Boundary-Layer Meteorology*, Kluwer Academic  
852 Publishers, Dordrecht, The Netherlands. Trebs, I., Bohn, B., Ammann, C., Rummel, U.,  
853 Blumthaler, M., Königstedt, R., Meixner, F. X., Fan, S., Andreae, M.O. (2009),  
854 Relationship between the NO<sub>2</sub> photolysis frequency and the solar global irradiance,  
855 *Atmospheric Measurement Techniques*, 2, 725–739

856 Turner, D.B.: *Workbook of atmospheric dispersion estimates*. 2nd ed., Lewis publisher,  
857 London, 175 p, 1994.

858 van Dijk, S., Meixner, F.X.: Production and consumption of NO in forest and pasture soils  
859 from the amazon basin, *Water Air Pollut.-Focus*, 1, 119–130, 2001.

860 van Dijk, S.M., Gut, A., Kirkman, G.A., Meixner, F. X., Andreae, M.O., Gomes, B. M.:  
861 Biogenic NO emissions from forest and pasture soils: relating laboratory studies to field  
862 measurements, *J. Geophys. Res.*, 107, LBA 25-1–LBA 25-11, doi:10.1029/2001JD000358,  
863 2002.

864 Vandaele, A.C. Hermans, C. Simon, P.C. Roozendael, M. Carleer, J.M. and Colin, R.: Fourier  
865 transform measurement of NO<sub>2</sub> absorption cross-section in the visible range at room  
866 temperature, *J. Atmos. Chem.*, 25, 289-305, 1996.

867 Volkamer, R., Spietz, P., Burrows, J., Platt, U.: High-resolution absorption cross-sections of  
868 glyoxal in the UV-vis and IR spectral ranges, *Journal of Photochemistry and Photobiology*  
869 *A: Chemistry*, 172 (1), 35-46, 2005.

870 Wagner, T., Ibrahim, O., Shaiganfar, R., Platt, U.: Mobile MAX-DOAS observation of  
871 tropospheric trace gases, *Atmos. Meas. Tech.*, 3, 129-140, 2010.

872 Wagner, T., Beirle, S., Brauers, T., Deutschmann, T., Frieß, U., Hak, C., Halla, J. D., Heue,  
873 K. P., Junkermann, W., Li, X., Platt, U., and Pundt-Gruber, I.: Inversion of tropospheric  
874 profiles of aerosol extinction and HCHO and NO<sub>2</sub> mixing ratios from MAX-DOAS  
875 observations in Milano during the summer of 2003 and comparison with independent data  
876 sets, *Atmos. Meas. Tech.*, 4, 2685-2715, doi:10.5194/amt-4-2685-2011, 2011.

877 Wittrock, F., Oetjen, H., Richter, A., Fietkau, S., Medeke, T., Rozanov, A., Burrows, J. P.:  
878 MAX-DOAS measurements of atmospheric trace gases in Ny-Ålesund – Radiative transfer  
879 studies and their application, *Atmos. Chem. Phys.*, 4, 955–966, 2004.

880 Yang, W. X., Meixner, F. X.: Laboratory studies on the release of nitric oxide from  
881 subtropical grassland soils: the effect of soil temperature and moisture, in: *Gaseous*  
882 *Nitrogen Emissions from Grasslands*, Wallingford, England, 67–70, 1997.

883 Yamulki, S., Goulding, K.W.T., Webster, C.P. and Harrison, R.M.: Studies on NO and N<sub>2</sub>O  
884 Fluxes from a Wheat Field, *Atmospheric Environment*, 29 (14), 1627–1635, 1995.

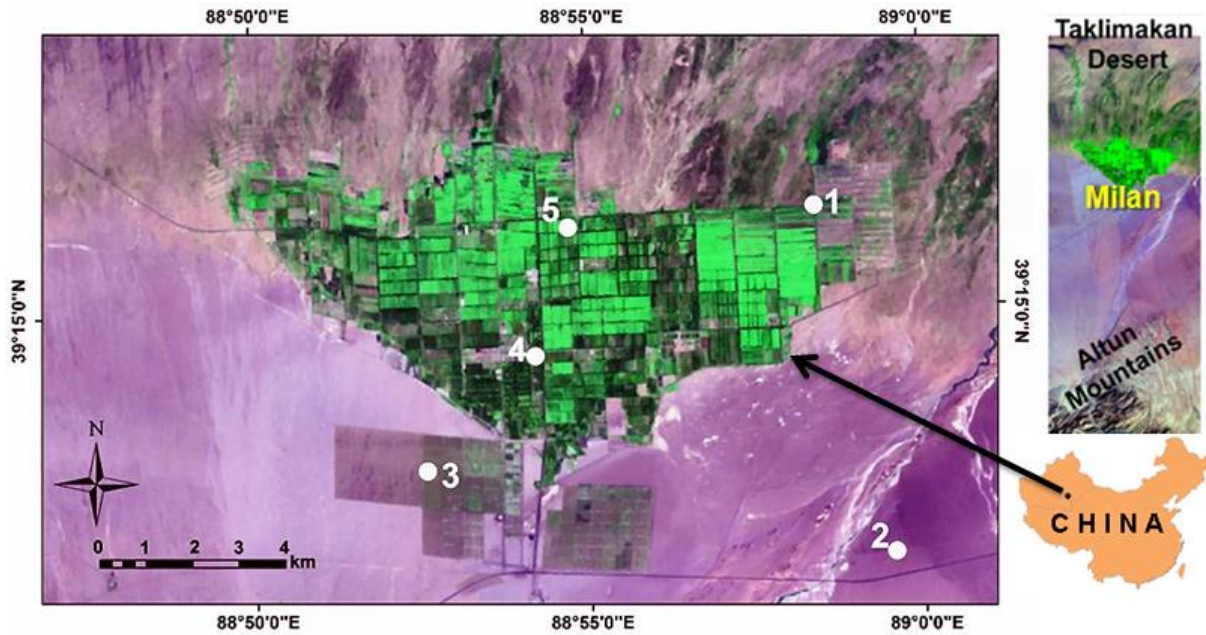
885 Yu, J., Meixner, F. X., Sun, W., Liang, Z., Chen, Y., Mamtimin, B., Wang, G., and Sun, Z.:  
886 Biogenic nitric oxide emission from saline sodic soils in a semiarid region, northeastern  
887 China: a laboratory study, *J. Geophys. Res.*, 113, 1–11, 2008.

888 Yu, J., Meixner, F. X., Sun, W., Mamtimin, B., Wang, G., Qi, X., Xia, C., and Xie, W.: Nitric  
889 oxide emissions from black soil, northeastern China: a laboratory study revealing  
890 significantly lower rates than hitherto reported, *Soil Biol. Biochem.*, 42, 1784–1792, 2010a.

891 Yu, J., Meixner, F.X., Sun, W., Mamtimin, B., Xia, C., Xie, W.: Biogenic nitric oxide  
892 emission of mountain soils sampled from different vertical landscape zones in the  
893 Changbai Mountains, Northeastern China, *Environ. Sci. Technol.*, 44, 4122–4128, 2010b.  
894

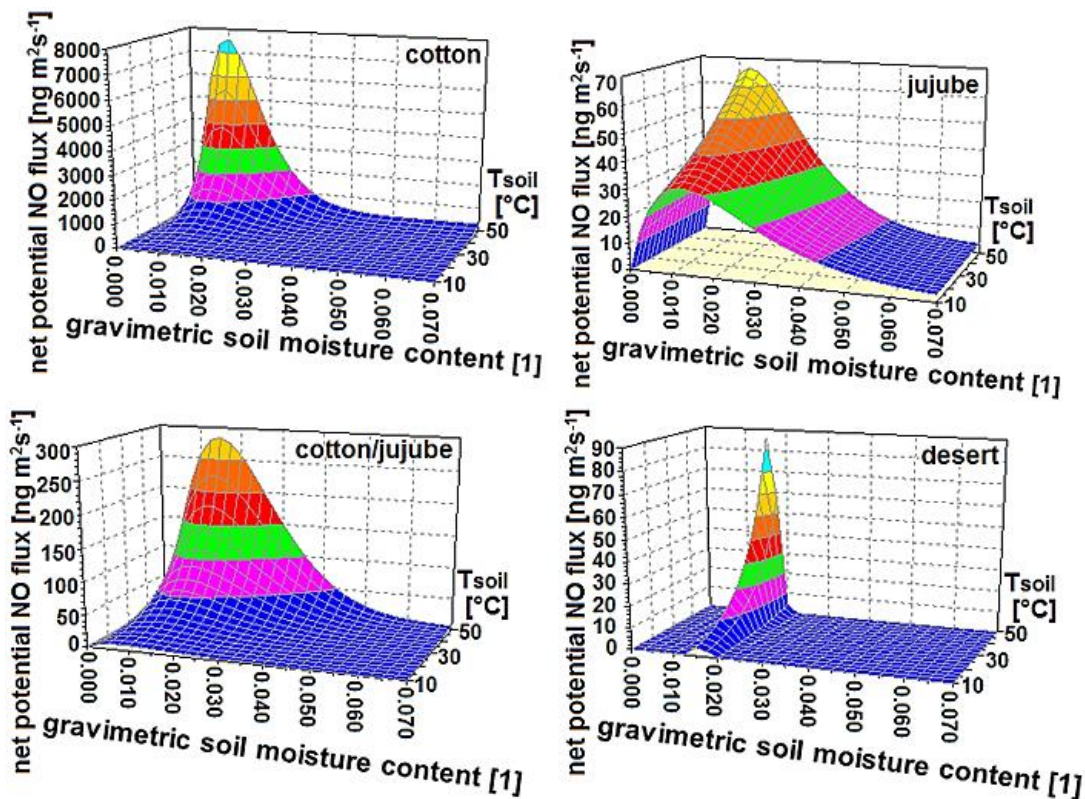
895

896 **Figures:**



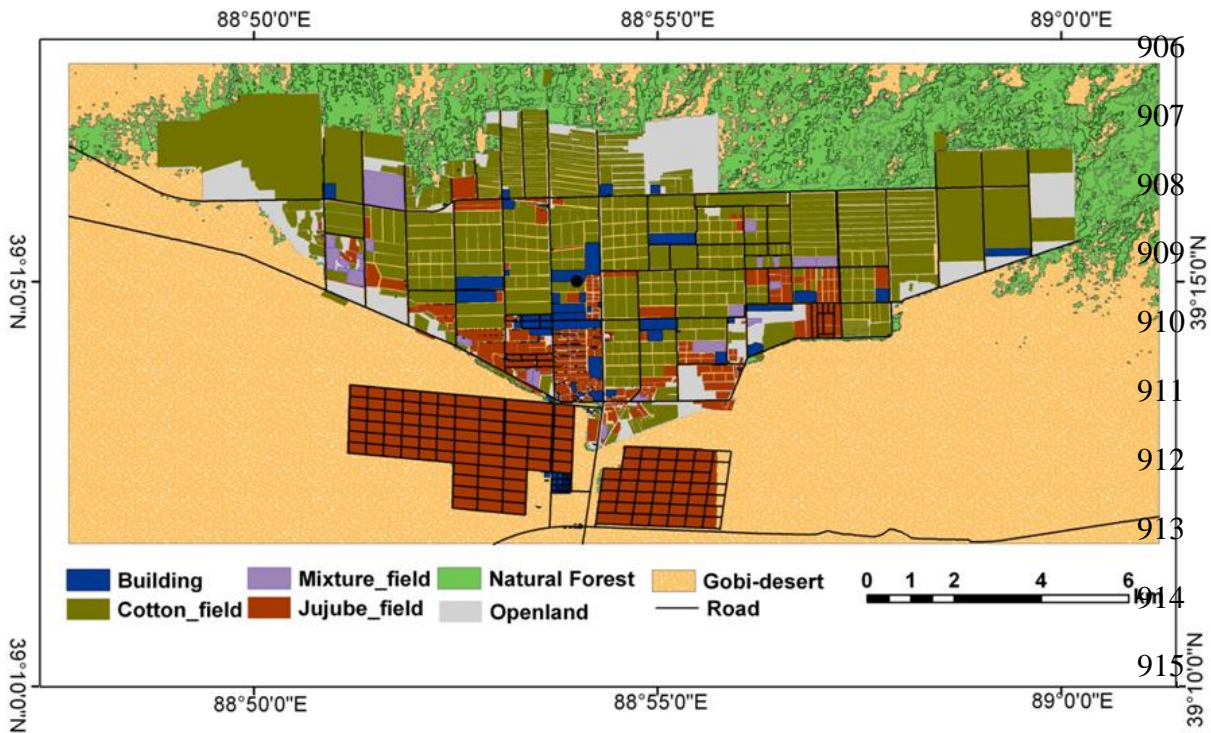
897

898 **Fig. 1:** Satellite map (Landsat ETM+; 2011) of Milan oasis, Xinjiang, NW-China (The map  
899 has an area of 338 km<sup>2</sup>). The white circles show the sites of *in-situ* measurements: natural  
900 forest (1), desert (2), jujube (3), hotel/oasis station (4) and cotton field (5).

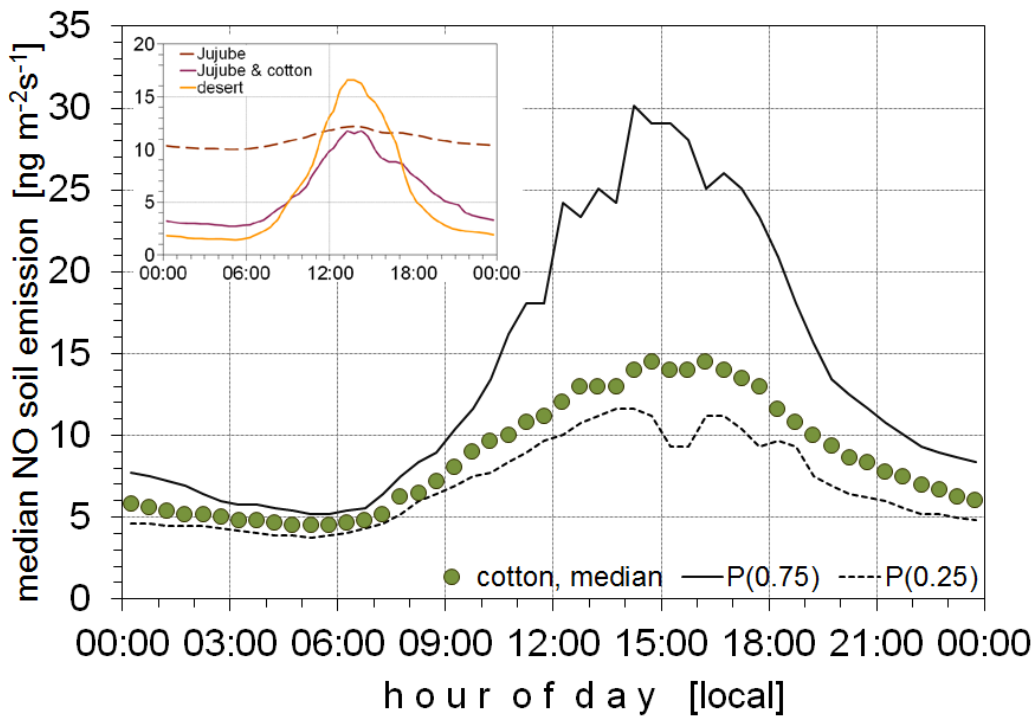


901

902 **Fig. 2:** Net potential NO fluxes  $F_{NO}$  (ng m<sup>-2</sup> s<sup>-1</sup>; in terms of mass of nitric oxide) from soils of  
903 the four major land-cover types of Milan oasis as functions of soil temperature (°C) and  
904 dimensionless gravimetric soil moisture content.

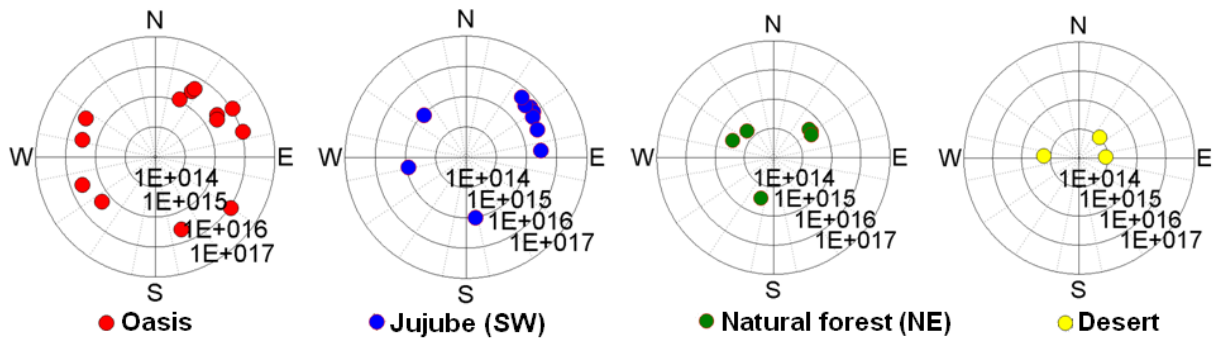


916 **Fig. 3:** 2011 map of land-cover types of Milan oasis as derived from satellite images  
 917 (Quickbird, Landsat ETM+, see Sect. 2.2.5).

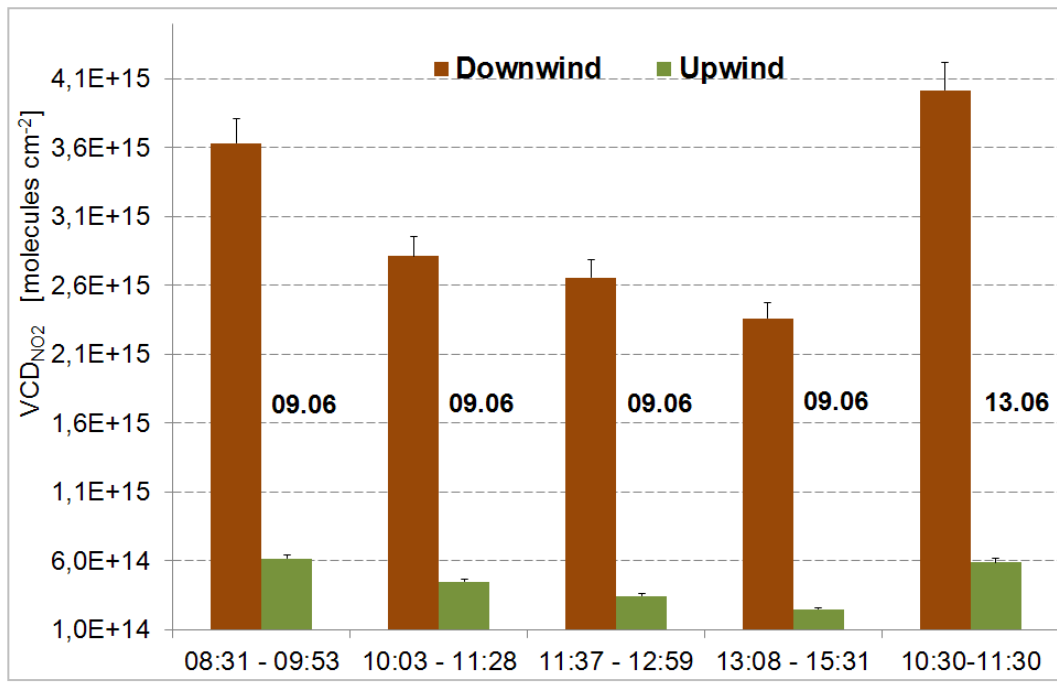


918  
 919 **Fig 4:** median diel variation of the actual NO-flux ( $\text{ng m}^{-2}\text{s}^{-1}$ ; in terms of mass of nitric oxide)  
 920 from soils of the four major land-cover types of Milan oasis for the period 03 to 24 June,  
 921 2011. Data have been calculated according eq.(10) using (a) soil temperatures (medians)  
 922 measured for each of the four major land-cover types, and (b) so-called “wilting point”-data  
 923 for corresponding soil moisture contents at the four sites (s. section 2.2.3). Data for the

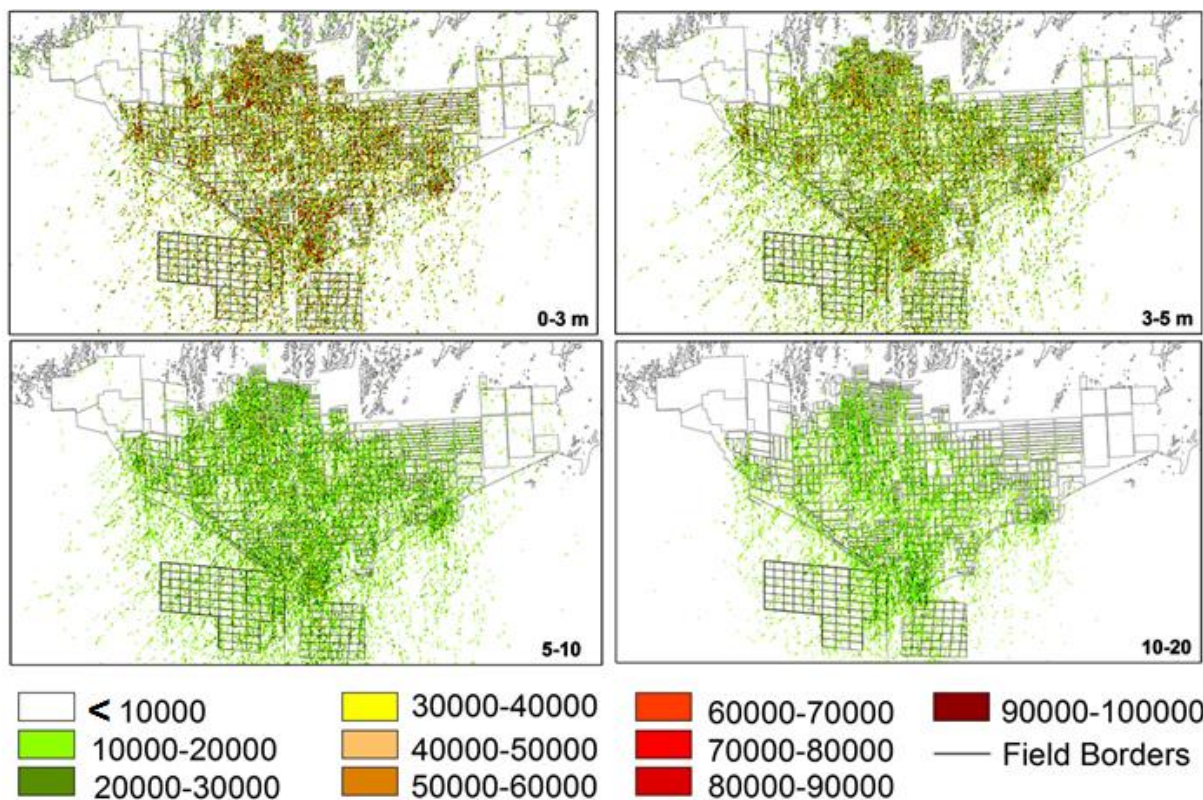
924 cotton-site are given as medians, as well as 25 and 75% quantiles, those for the Jujube,  
 925 Jujube-cotton and desert sites as medians only (s. figure insert).



926  
 927 **Fig. 5:** Results of MAX-DOAS measurements performed at sites oasis/hotel (4), Jujube (3),  
 928 Natural forest (1), and Desert (2) of Milan oasis from 23 May to 26 June, 2011 (see Fig. 1).  
 929 Vertical  $\text{NO}_2$  column densities (in molecules  $\text{cm}^{-2}$ ; 20-30 min averages) are shown in relation  
 930 to in-situ measured wind direction at each location of MAX-DOAS measurements. The  
 931 MAX-DOAS measurements were performed between 6:00 and 19:00 (local time). Note the  
 932 radial logarithmic scale of VCD data.



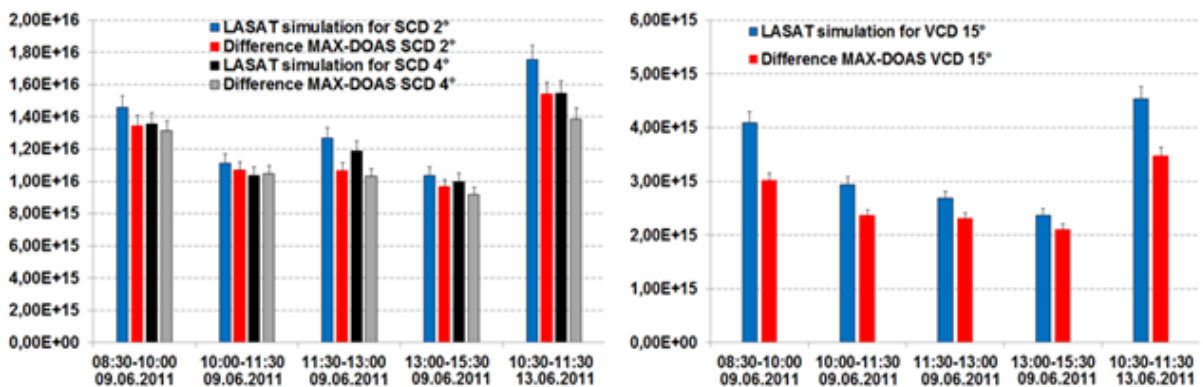
945 **Fig. 6:** Results of  $\text{NO}_2$ -VCD measured simultaneously with two MAX-DOAS instruments up-  
 946 upwind (natural forest, site (1)) and downwind (jujube field, site (3)) of Milan oasis on 09 and  
 947 13 June, 2011.



948

949 **Fig. 7:** Results of NO concentrations ( $\text{ng m}^{-3}$ ; in terms of mass of nitric oxide) calculated by  
 950 the LASAT dispersion model for the first four vertical levels on 09 June, 2011, 11:30 to 13:00  
 951 (local time).

952



953

954 **Fig. 8:** Simulated SCDs vs. SCDs measured by MAX-DOAS (a) and simulated VCDs vs.  
 955 VCDs measured by MAX-DOAS (b) on 09 and 13 June, 2011 at Milan oasis. SCDs have  
 956 been measured and simulated for elevation angles of 2° and 4°, VCDs were measured at 15°.

957

958